Science and Technology of Advanced Materials

ISSN: (Print) (Online) Journal homepage: www.tandfonline.com/journals/tsta20

Structures, fundamental properties, and potential applications of low-dimensional C_{60} polymers and other nanocarbons: a review

Jun Onoe, Yusuke Noda, Qian Wang, Koji Harano, Masato Nakaya & Tomonobu Nakayama

To cite this article: Jun Onoe, Yusuke Noda, Qian Wang, Koji Harano, Masato Nakaya & Tomonobu Nakayama (2024) Structures, fundamental properties, and potential applications of low-dimensional C_{60} polymers and other nanocarbons: a review, Science and Technology of Advanced Materials, 25:1, 2346068, DOI: 10.1080/14686996.2024.2346068

To link to this article: https://doi.org/10.1080/14686996.2024.2346068

Published online: 20 May 2024.

SCIENCE AND TECHNOLOGY OF ADVANCED MATERIALS
2024, VOL. 25, NO. 1, 2346068
https://doi.org/10.1080/14686996.2024.2346068

Structures, fundamental properties, and potential applications of low-dimensional C_{60} polymers and other nanocarbons: a review

Jun Onoe[a], Yusuke Noda[b]*, Qian Wang[c], Koji Harano[d], Masato Nakaya[a] and Tomonobu Nakayama[d]

[a]Department of Energy Science and Engineering, Nagoya University, Nagoya, Japan;
[b]Department of Information and Communication Engineering, Okayama Prefectural University, Soja, Japan;
[c]School of Materials Science and Engineering/Center for Applied Physics and Technology, Peking University, Beijing, China;
[d]Center for Basic Research on Materials, and Division of International Collaborations and Public Relations, National Institute for Materials Science (NIMS), Tsukuba, Japan

ABSTRACT

Since carbon (C) atom has a variety of chemical bonds *via* hybridization between s and p atomic orbitals, it is well known that there are robust carbon materials. In particular, discovery of C_{60} has been an epoch making to cultivate nanocarbon fields. Since then, nanocarbon materials such as nanotube and graphene have been reported. It is interesting to note that C_{60} is soluble and volatile unlike nanotube and graphene. This indicates that C_{60} film is easy to be produced on any kinds of substrates, which is advantage for device fabrication. In particular, electron-/photo-induced C_{60} polymerization finally results in formation of one-dimensional (1D) metallic peanut-shaped and 2D dumbbell-shaped semiconducting C_{60} polymers, respectively. This enables us to control the physicochemical properties of C_{60} films using electron-/photo-lithography techniques. In this review, we focused on the structures, fundamental properties, and potential applications of the low-dimensional C_{60} polymers and other nanocarbons such as C_{60} peapods, wavy-structured graphene, and penta-nanotubes with topological defects. We hope this review will provide new insights for producing new novel nanocarbon materials and inspire broad readers to cultivate new further research in carbon materials.

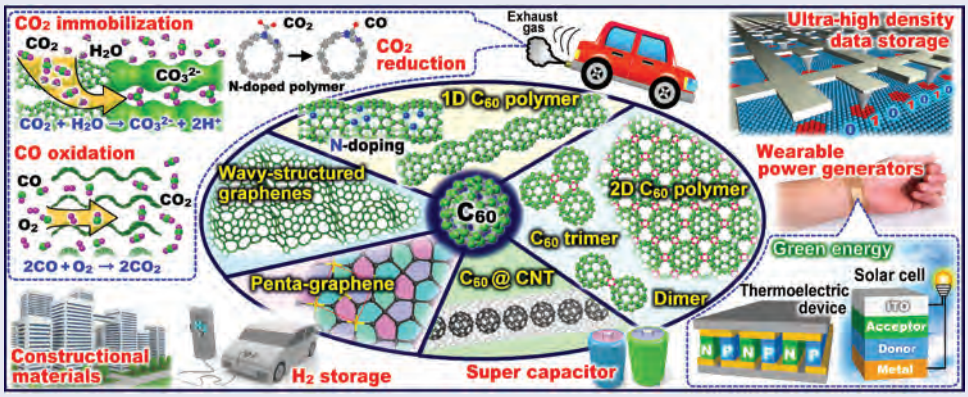

ARTICLE HISTORY
Received 15 March 2024
Revised 16 April 2024
Accepted 17 April 2024

KEYWORDS
Low dimensional nanocarbons; structures; fundamental properties; potential applications

IMPACT STATEMENT

We review the structures, fundamental properties, and applications of low-dimensional C_{60} polymers and other related nanocarbons such as C_{60} peapods, wavy-structured graphene, and penta-nanotubes from a standpoint of topological defects.

1. Introduction

Since the discovery of low-dimensional carbon materials such as zero-dimensional C_{60} [1], one-dimensional (1D) carbon nanotubes (CNTs) [2], and 2D graphene [3] from the end of the 20th century to the beginning of the 21st century, they are well known to have cultivated new science and industrial applications so far [4–6].

Since C_{60} has unique features such as solubility (against organic solvents such as toluene) and volatility (Chap. 5 of Ref. [4]), it is easy to produce C_{60} films on any substrate using spin-coat or thermal

CONTACT Jun Onoe j-onoe@energy.nagoya-u.ac.jp Department of Energy Science and Engineering, Nagoya University, Furo-cho, Chikusa-ku, Nagoya, Aichi 464-8603, Japan

*Present address: Department of Physics and Information Technology, Kyushu Institute of Technology, Kawazu, Iizuka, Fukuoka 820–8502, Japan.

evaporation method, which is advantage for device fabrication. In addition, the electric conductivity of C_{60} films can be controlled from insulating to semiconducting/metallic using photo/electron-induced polymerization (Chap. 7 of Ref. [4]) with a variety of cross-linked structures based on the generalized Stone-Wales (GSW) transformation [7] in association with topological defects. Figure 1 shows schematic representation of the change in geometrical structure from dumbbell-shaped C_{60} dimer to C_{120} nanotube *via* the GSW transformation [7] in association with topological defects. Although the other polymerization methods such as high-pressure/high-temperature (HPHT) treatment [10], alkali-metal doping [11], and mechanochemical reaction [12] are also well known so far, these methods are however hard to be employed practically in device fabrication processes. On the other hand, since photolithography and electron-beam (EB) lithography are well known to be a standard technique for many semiconductor devices, the modification of the physicochemical properties by photo/electron-induced polymerization is useful to improve the device performance such as solar cells [13].

From this standpoint, Onoe et al. have hitherto investigated the structural and physicochemical properties of photo- and electron-beam (EB)-induced polymerized C_{60} films under ultrahigh vacuum (UHV) conditions [14,15], and demonstrated that photopolymerization finally results in formation of a 2D semiconducting dumbbell-shaped C_{60} polymer [16–20], whereas EB-polymerization finally results in formation of a 1D metallic uneven-structured (peanut-shaped) C_{60} polymer [21–26] *via* the GSW transformation [7], as shown in Figure 2 [20].

In this review, we will introduce the structures, fundamental properties, and potential applications of 1D peanut-shaped C_{60} polymer and related materials formed *via* electron-induced polymerization in Section 2, and those of 2D dumbbell-shaped C_{60} polymer and related materials formed *via* photo-induced polymerization in Section 3. Thereafter, we will introduce the other low-dimensional nanocarbon materials such as C_{60} peapods, wavy-structured graphenes, and penta-nanotubes in Section 4. Finally, we will describe the outlook for future research in nanocarbon materials in Section 5. Although nanodiamonds are regarded as quantum dots, there have been many review papers so far [27–29]. Thus, they are omitted in this review.

2. One-dimensional peanut-shaped C_{60} polymers and related nanocarbons formed *via* electron-induced polymerization

2.1. Structures

Onoe et al. have examined the cross-linked structure of 1D C_{60} polymer using *in situ* Fourier-transform infrared (FT-IR) spectroscopy in combination with first-principles calculations based on density

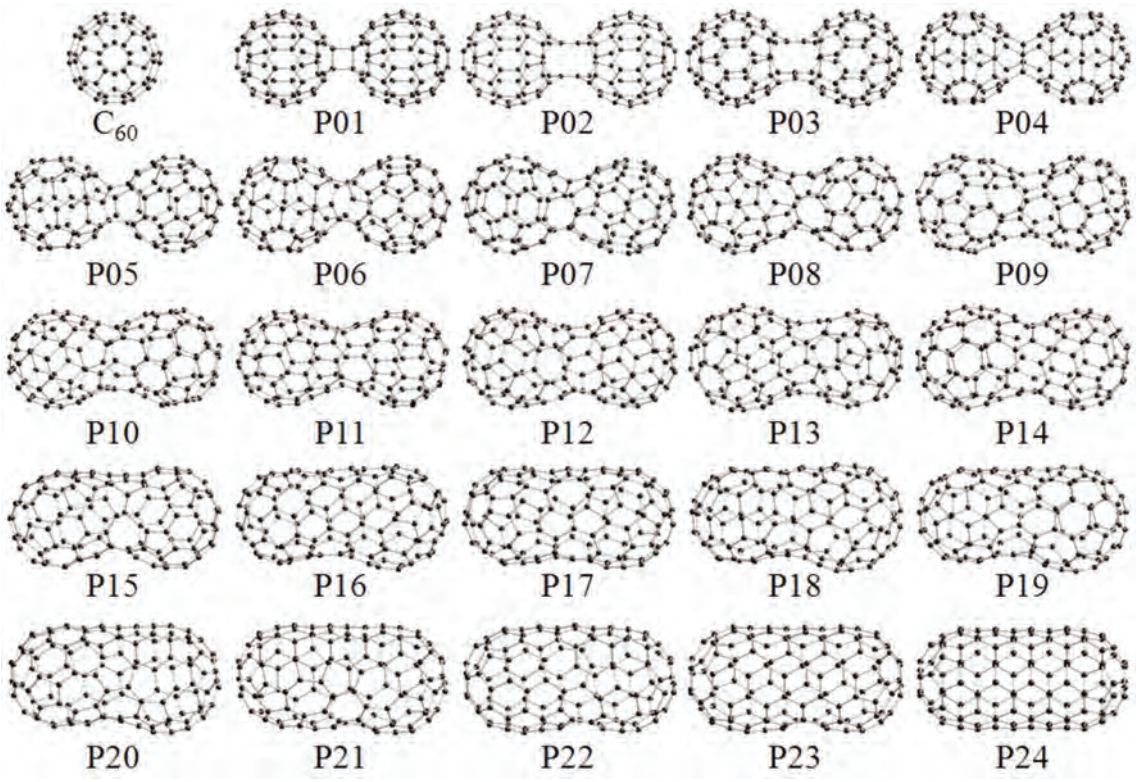

Figure 1. Schematic representation of the change in geometrical structure from C_{60} dimer (P01) to C_{120} nanotube (P24) *via* the general Stone-Wales transformation [8]. The structures of P01–P24 derived from the GSW transformation [7] were geometrically optimized using Gaussian03 package [9]. Takashima et al. [8]; licensed under a Creative Commons Attribution (CC BY) license.

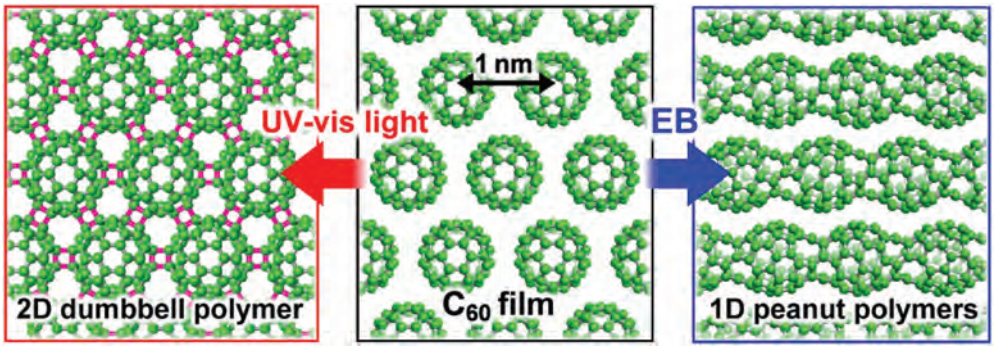

Figure 2. Schematic illustration of pristine C_{60} film (center), 2D semiconducting dumbbell-shaped C_{60} polymer network (left), and 1D metallic uneven-structured (peanut-shaped) C_{60} polymer chain (right) [20]. Onoe et al. [20]; licensed under a Creative Commons Attribution (CC BY) license.

functional theory (DFT) [8]. Comparison between the experimental and theoretical IR spectra suggests that the cross-linked structure of the 1D peanut-shaped C_{60} polymer is roughly close to that of P08 *via* intermediate cross-linkages of P01, P04, and P06 (see Figure 1) [30]. Since the IR peaks originating from the 1D polymer are intense and narrow (the full width at half maximum is almost same as that of pristine C_{60} film), the cross-linkage is considered to be one given structure.

Masuda et al. further examined the 1D polymer obtained from electron-beam irradiated C_{60} single crystal (SC) films using high-resolution transmittance electron microscope (HRTEM). Judging from the cryo-HRTEM images and their corresponding fast Fourier-transformed (FFT) patterns [26] in comparison with the results of electron diffraction pattern [25], they demonstrated the structural change from pristine C_{60} SC film to 1D C_{60} polymer film by EB irradiation, as shown in Figure 3. Here, the unit cell of (a) and (b) is shown by a red solid line. C_{60} molecules in the three-fold symmetrical $[111]_{FCC}$ layer (Figure 3(a)) are polymerized to form the 1D C_{60} polymer $[0001]_{HCP}$ with an intermolecular distance of 0.93 nm along one of the three nearest neighboring directions of $[-12-10]_{HCP}$ in association with the symmetry broken to change the stacking from FCC to HCP-m (Figure 4(b)). Here, FCC and HCP are the abbreviation of 'face-centered-cubic' and 'hexagonal-closed-pack', respectively.

2.2. Fundamental properties

The 1D peanut-shaped C_{60} polymer with a concave-convex periodic curved structure exhibited physical properties arising from 1D metal such as Peierls transition [31], charge-density-wave phonon anomaly [32], and 1D van Hove singularity of phonon dispersion [33]. Especially, it is interesting to note that the 1D polymer film first demonstrates

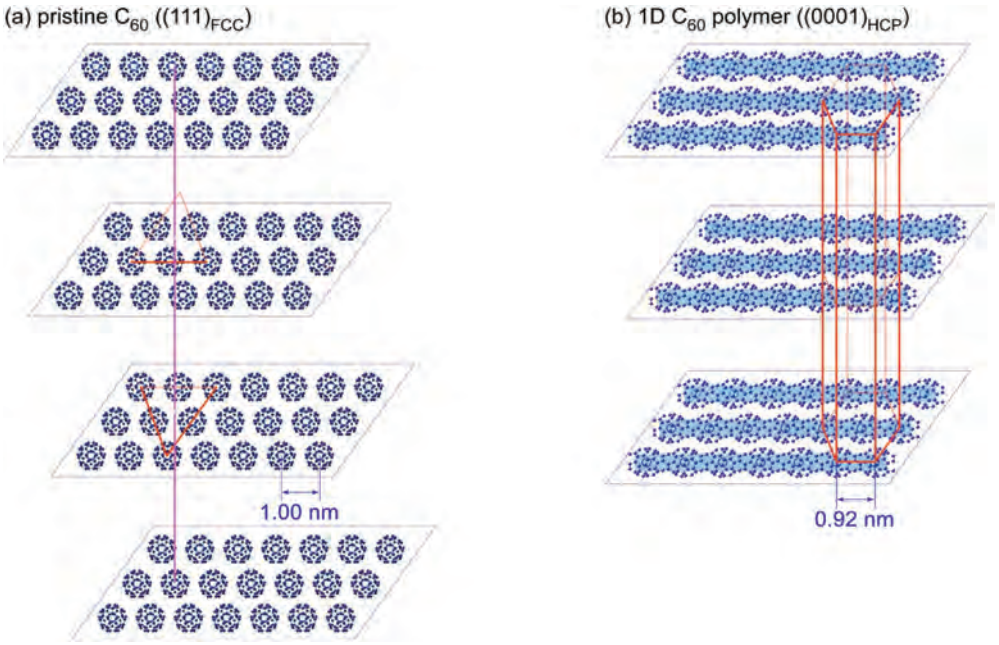

Figure 3. Schematic illustration of (a) face-centered-cubic (FCC) C_{60} structure model and (b) hexagonal-closed-pack (HCP) structure model for 1D C_{60} polymer [26]. Here, blue band lines shown in FIG. (b) Show the direction of 1D C_{60}–C_{60} polymerization. Masuda et al. [26]; licensed under a Creative Commons Attribution (CC BY) license.

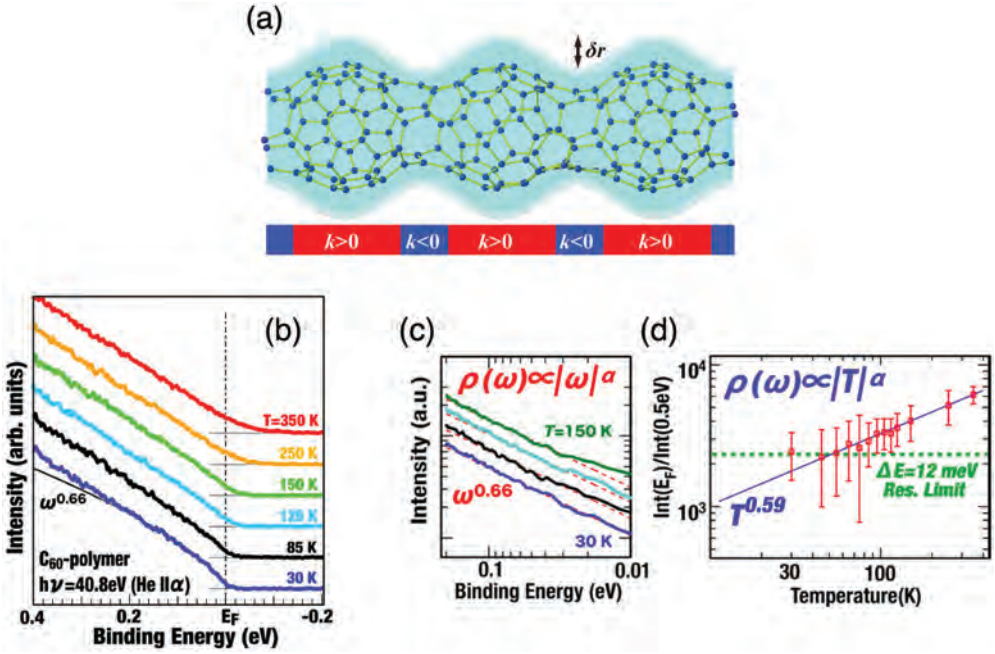

Figure 4. (a) Schematic illustration of the 1D metal C_{60} polymer with an uneven peanuts-shaped structure similar to the cross-linked structure of the P08 C_{120} stable isomer shown in Figure 1. The area colored in sky blue represents a geometrical curved surface in which π-electrons move one-dimensionally. The δr denotes the degree of uneven deformation. (b) Temperature dependence of the photoelectron spectra of the 1D peanut-shaped C_{60} polymer in the vicinity of E_F. (c,d) The power-law dependence of the photoelectron spectral function shown in (b) on the binding energy (c) and temperature (d) [24]. Onoe et al. [24]; licensed under a Creative Commons Attribution (CC BY) license.

geometrical curvature effects on the electronic states [24,34], which has been a big puzzle in quantum mechanics since the theoretical predictions in 1950s [35–37].

The behavior of the free electrons on the curved surface is characterized by the Hamilton operator of the following equation (quantum mechanics of sub-manifold),

$$\hat{H} = -\frac{\hbar^2}{2m^*}\left[\frac{1}{\sqrt{g}}\sum_{i,j=1}^{2}\frac{\partial}{\partial q^i}\left(\sqrt{g}g^{ij}\frac{\partial}{\partial q^j}\right) + \left(h^2 - k\right)\right]$$

Here, m^* is the effective mass of the electron, (q^1, q^2) is the curved coordinate system, g^{ij} is the inverse matrix component of matrix [g_{ij}], g is the determinant of matrix [g_{ij}], and g_{ij} is the metric tensor, respectively. h and k are the mean curvature and Gaussian curvature, respectively, and represent the degree of curvature at each point on the curved surface. Since h and k are the functions of g_{ij}, the Hamilton operator is uniquely determined by g_{ij} describing a shape once the shape of the surface is determined. It is worth noting that the second term appears as a new scalar potential [Jensen-Koppe-da Costa (JKC) potential] besides the first term corresponding to the kinetic energy of the electron. This is the effective electric field potential caused by the geometric curvature of the surface, and plays a role in driving surface-curvature induced changes in physical properties.

The 1D peanut-shaped polymer exhibits Tomonaga-Luttinger liquid (TLL) states [38,39] which is the direct evidence for 1D metal [24]. Accordingly, the density-of-states (DOS: ρ) of 1D metal obey not Fermi-Dirac distribution function but a power-law dependence of binding energy or temperature when measured using photoelectron spectroscopy. Namely,

$$\rho(E) \propto |E - E_F|^{\alpha} \text{ or } \rho(E) \propto |T|^{\alpha}$$

Here, E, E_F, and T denote binding energy, Fermi energy, and absolute temperature, respectively. When the exponent α is less than unity (α < 1), it can be regarded as 1D metal with TLL states. Actually, 1D metallic single wall (SW) CNTs show a power-law dependence with an exponent (α) of ca. 0.5 [40].

As shown in Equation 1, to demonstrate whether the JKC potential affects the electronic states or not, Shima et al. first theoretically examined the change in the α using deformed cylinder models (Figure 1 of Ref. [34]), whose radius varies periodically, and found that the variation in the surface curvature inherent to the system gives rise to a significant increase in the power-law exponent of the single-particle DOS (Figure 5 of Ref. [34]).

Onoe et al. examined the exponent α of 1D peanut-shaped C_{60} polymer film using *in situ* high-resolution photoemission spectroscopy (PES) [24]. As shown in Figure 4(a), the 1D peanut-shaped C_{60} polymer shows a power-law dependence at 30 K, which indicates TLL

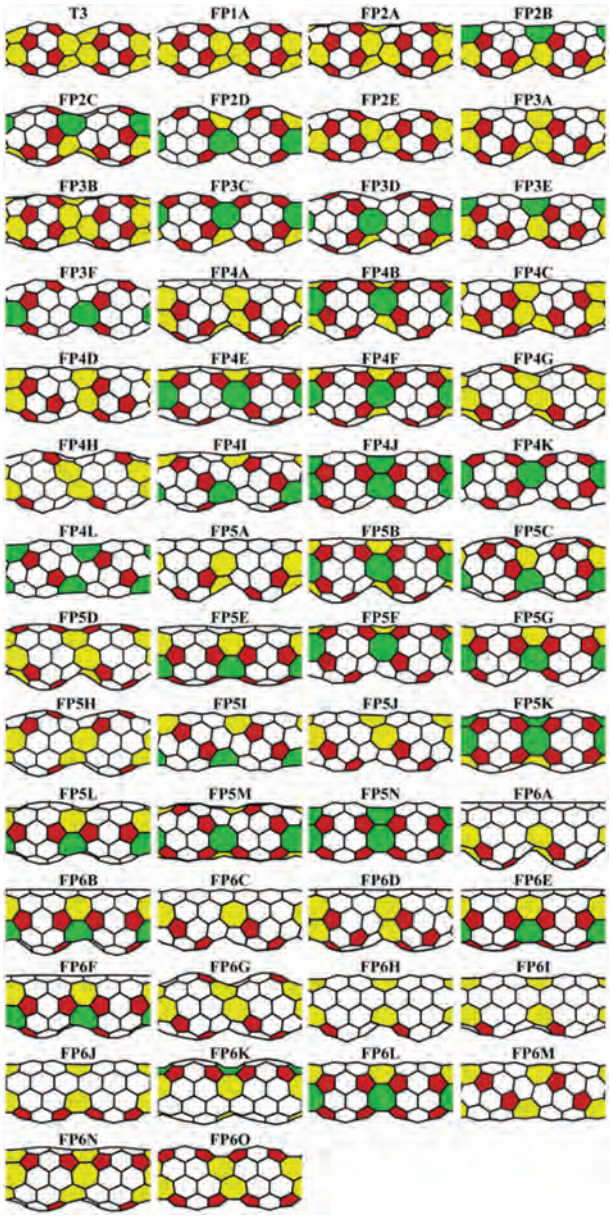

Figure 5. Geometrical structures of 54 different 1D peanuts-shaped C_{60} polymer models. Red, white, yellow, and green carbon-network polygons indicate 5-, 6-, 7-, and 8-membered rings, respectively [41]. Reprinted with permission from Noda et al. [41]. Copyright 2015 American Chemical Society.

states in case of 1D metal. By fitting the PES spectra with a power-law function of Equation 2 in the energy range of 18–70 meV, they obtained an exponent α of 0.66, as shown in Figure 4(c). Since the TLL exponent α value depends on the choice of an energy range set for fitting, they examined various energy range sets within 18–100 meV (a fitting accuracy of ±0.02) and obtained α to be 0.65 ± 0.08. In a similar manner, Figure 4(d) plots the temperature dependence of the ratio of the photoemission intensity at E_F to the intensity at 0.5 eV in binding energy on a log – log scale, and demonstrates a power-law dependence on temperature in the range of 30–350 K, in which the exponent α was obtained to be 0.59 ± 0.04. Judging from the results of Figure 4, the TLL exponent α for the 1D peanut-shaped C_{60} polymer can be concluded to be ca. 0.6, which is significantly larger than that of ca. 0.5 (0.43–0.54) for metallic SWCNTs [40,42,43]. In the theoretical work [34], when the radial modulation degree (δr) of the uneven structure increased from 0 nm (a straight tube) to 0.16 nm (an uneven peanut-shaped tube), the TLL exponent α increased from 0.5 to 0.6. As shown in Figure 4(a), the δr can be estimated to be ca. 0.14 nm, which is in good agreement with the predicted value. Details of discussion have been described in Ref. [22]. Thus, Onoe et al. first observed the geometrical curvature effects on electronic states that have been a big puzzle since 1950s. This is a novel property different from that of fullerenes, CNTs, and graphene.

It is important to consider the heat-resistance of the 1D peanut-shaped C_{60} polymer for practical use. Nakaya et al. confirmed that the 1D polymer exhibits a heat-resistance at least up to 723 K annealing under UHV conditions [44], because the thermal heating system thus used can rise temperatures up to 723 K. This is comparable to that of polyimide film commercially available as the highest heat-resistance organic material.

In addition to the 1D peanuts-shaped C_{60} polymer described above, electronic properties of the other peanut-shaped C_{60} polymers have been investigated theoretically [45–47]. Noda et al. performed first-principles calculations of several 1D peanut-shaped C_{60} polymer models to examine their energetically stable structure and electronic properties [41]. Figure 5 shows schematic illustration of 54 different 1D peanut-shaped C_{60} polymer models optimized geometrically (T3 model was proposed by G. Wang et al. [45], and the other 53 models were derived from the T3 model *via* the GSW transformation). They consist of not only 5-/6- but also 7- and/or 8-membered rings. Unlike 1D CNTs consisting of only 6-membered ring, the 1D peanut-shaped C_{60} polymer models have both positive and negative Gaussian curvatures respectively caused by the 5- and 7/8-membered rings beside 6-membered one. It is found from the results of Figure 5 that the FP5N model is most stable energetically among the 54 models (see Table 1 of Ref. [41]). Interestingly, the energetic stability of the 1D peanut-shaped C_{60} polymers depends on their geometric components: the more octagon and pentagon-octagon pairs (heptagon and hexagon-heptagon pairs) in their structures, the more stable (unstable) the 1D polymers.

Figure 6 shows the band structures of typical 1D peanut-shaped C_{60} polymer models (T3, FP4K, FP5N, and FP6L) chosen among the 54 different models, and indicates that the metallic or semiconducting band structure of the 1D peanut-shaped C_{60} polymers depends on their carbon-network polygon patterns. Especially, the band

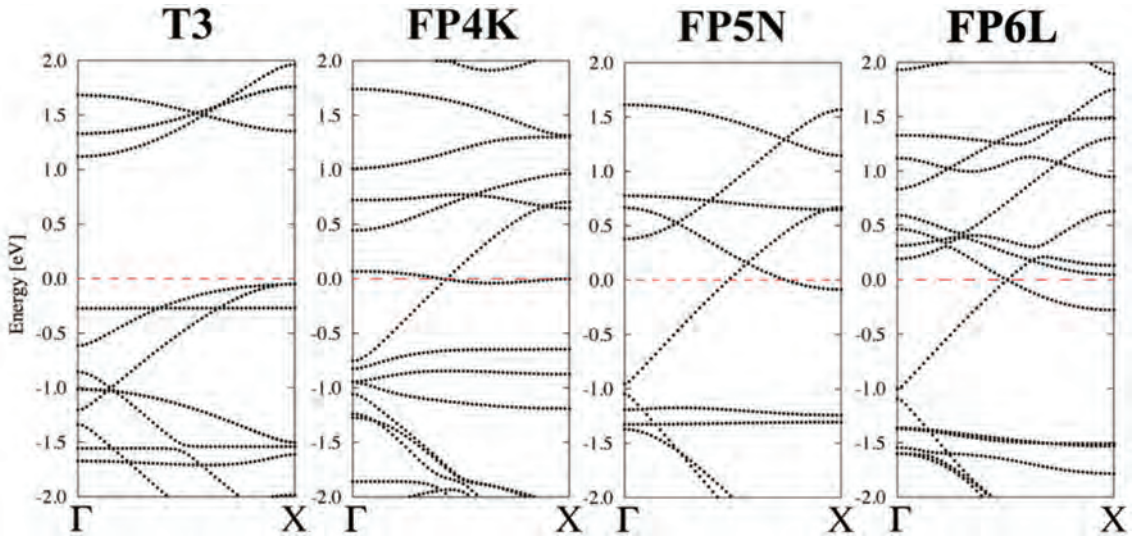

Figure 6. Band structures of T3, FP4K, FP5N, and FP6L polymer models shown in Figure 5. Here, the horizontal dashed red line indicates the Fermi level [41]. Reprinted with permission from Noda et al. [41]. Copyright 2015 American Chemical Society.

structure of the FP5N model with the lowest total energy shows a metallic property (no band gap near E_F).

2.3. Potential applications

2.3.1. Ultrahigh density reversible memory atomically controlled by STM

Shrinkage in the intermolecular distances (center-to-center distance) by ca. 0.1 nm when two C_{60} molecules form a dumbbell-shaped dimer [4] is required to be detected in real space using atomic force microscope (AFM) [48] and STM [49]. This fact leads to readily discriminate C_{60} monomers and its dimers, and gives rise to utilize the dimers as a carrier of digital information representing '1', whereas the monomers as that representing '0'. Thanks to the 1 nm size of a single C_{60} molecule, when a C_{60} dimer is used as a digital bit, it is expected that the density of digital bits reaches to more than tens of terabits per square inches ideally. This meets with the information-oriented society requiring innovative data storage technologies [50,51].

Utilizing molecular thin films as a recording media has been extensively proposed and investigated so far [52–61]. When compared to other molecules, it is noted that C_{60} molecule has following three advantages. Firstly, C_{60} molecule and its thin film are relatively stable and easy to be handled in both dry and wet processes. Secondary, well-ordered high-purity C_{60} thin films are easily produced on any substrate at RT. Thirdly, C_{60} polymerization/depolymerization in its thin film can be controlled reversibly and locally at designated positions with a nanometer precision [53,55] using STM as described below.

To control the number of C_{60} molecules chemically bound with each other at nanoscale, local excitation is a promising way. Electronic excitation or field ionization induced by atomically sharp STM tip [62–64] has been found to control the polymerization/depolymerization area at a single C_{60} scale [53,55,60,65]. For examples, Nakayama's group examined STM tip-induced dimerization/de-dimerization in a C_{60} monolayer on a highly oriented pyrolytic graphite (HOPG) [65]. Figure 7(a) shows a series of STM images acquired at a sample bias voltage (V_s) of +1.0 V and a tunneling current (I_t) of 20 pA in the same area at RT: pristine C_{60} monolayer (left), dimerization (center) induced by negative (−2.7 V) *Vs* with a pulse width of 1 s, and de-dimerization (right) induced by positive (+3.0 V) *Vs* with a pulse width of 1 s. Since C_{60} molecule is freely rotated on an inert substrate such as HOPG, STM image of the molecule shows a spherical. On the other hand, since C_{60} dimer with [2 + 2] four-membered cross-linkage is stopped rotating, STM image of the dimer shows a stripe with an internal structure [49].

Figure 7(b) shows the mesh imposed to the STM image after the dimerization (left) and schematically illustrates the corresponding dimerization (right). A slight shift in the molecular position of C_{60} dimer can be measured from the STM images [49,65].

They further examined STM images of the intermolecular bonds between C_{60} molecules in a multilayer film [53], and found that the probability of polymerization/depolymerization was higher than that in a monolayer film, because all the C_{60} molecules in a monolayer inevitably interact with the underlying substrate surface more or less. In case of a C_{60} trilayer film, the intermolecular distance in the dimer was estimated to be 0.9 nm [66], which is in good agreement with that of a dimer *via* the [2 + 2] cycloaddition reaction between C_{60} molecules [12,49,67–69]. Furthermore, it is noted that C_{60} trimers were also observed besides the dimers.

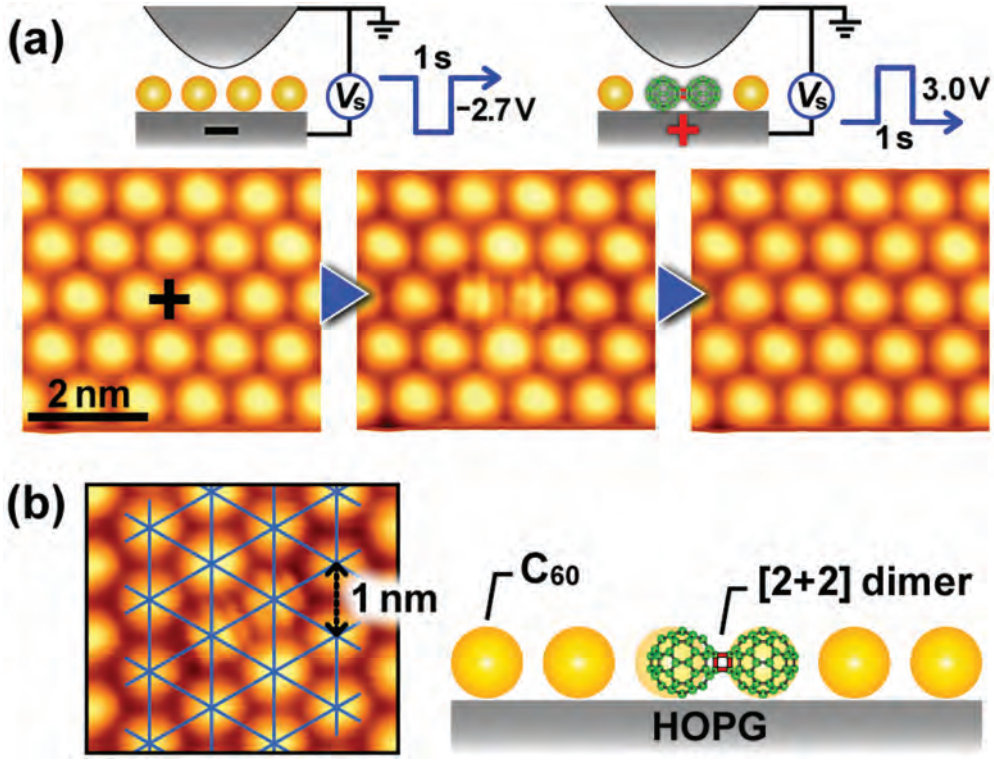

Figure 7. (a) High-resolution STM images showing control of polymerization (left to central) and depolymerization (central to right) between C_{60} molecules in C_{60} monolayer film using STM. (b) Local modification of molecular arrangement in C_{60} monolayer films after polymerization [65,65]. Superimposed triangular mesh in left STM image shows two-dimensional periodicity of pristine C_{60} molecules. Right picture shows schematic side view of a C_{60} dimer in the monolayer film.

Figure 8 shows that the unbound (a) and bound (b) states of C_{60} molecules can be controlled locally and selectively just below the STM tip at RT only by changing the polarity of the V_s. The high selectivity and reversible control between the monomer and polymer performed at RT is a specific feature of STM-induced C_{60} polymerization/depolymerization when compared to alternative methods such as high-temperature/high-pressure [10], photo-irradiation [70], and alkali-metal doping [11]. The reason behind such the high selectivity is due to the electric-field-induced shifts in the molecular orbital energy levels associated with charge transfer to/from substrate, namely, ionization of C_{60} molecules caused underneath the STM tip (Figure 8(c,d)). More details of the physical mechanisms of the selective induced polymerization/depolymerization have been theoretically investigated using first-principles calculations [68].

When we consider potential applications of polymerization/depolymerization control to memory devices and further to data storage technology, the density of digital bits, the speed of bit operations, and the nonvolatility of the bits play key roles in these applications. Since there have hitherto been some reports on improvement of the three key factors toward realization of polymerization/depolymerization-based data storage technologies, we will overview the status of those developments as below.

Data-storage centers are relying on the performance of magnetic hard disk drive (HDD), and it is highly demanded to increase the capacity of the data center by a higher density storage technology [53]. Tremendous work has been devoted to increase the capability of magnetic recording technology. However, since there is a certain physical limitation coming from magnetic instability when decreasing the size of a bit, a lot of studies have been carried out for future data-storage devices beyond magnetic devices so far. Kalff et al. demonstrated an example of ultrahigh density data-storage using positional operation of single chlorine atoms on Cu(100) by STM [71], and achieved a bit density of 3.2 Pbits/inch^2 (P: peta-; $\times 10^{15}$). However, the operation of bits and keeping the bit status require ultrahigh vacuum and low-temperature conditions (bit operation was demonstrated at 1.5 K). Deoxyribonucleic acid (DNA) molecules have also been investigated by Church et al. and Erlich et al., because they have a potential to provide a huge-capacity for store data [72,73]. Although the information density of DNA-based storage device is expected to be 10^5 times larger than that of HDD [72], essential digital operations such as DNA sequencing (encoding) and reading (decoding) is still impractical in time and costs [73].

On the other hand, an ultrahigh density data storage based on local C_{60} polymerization/

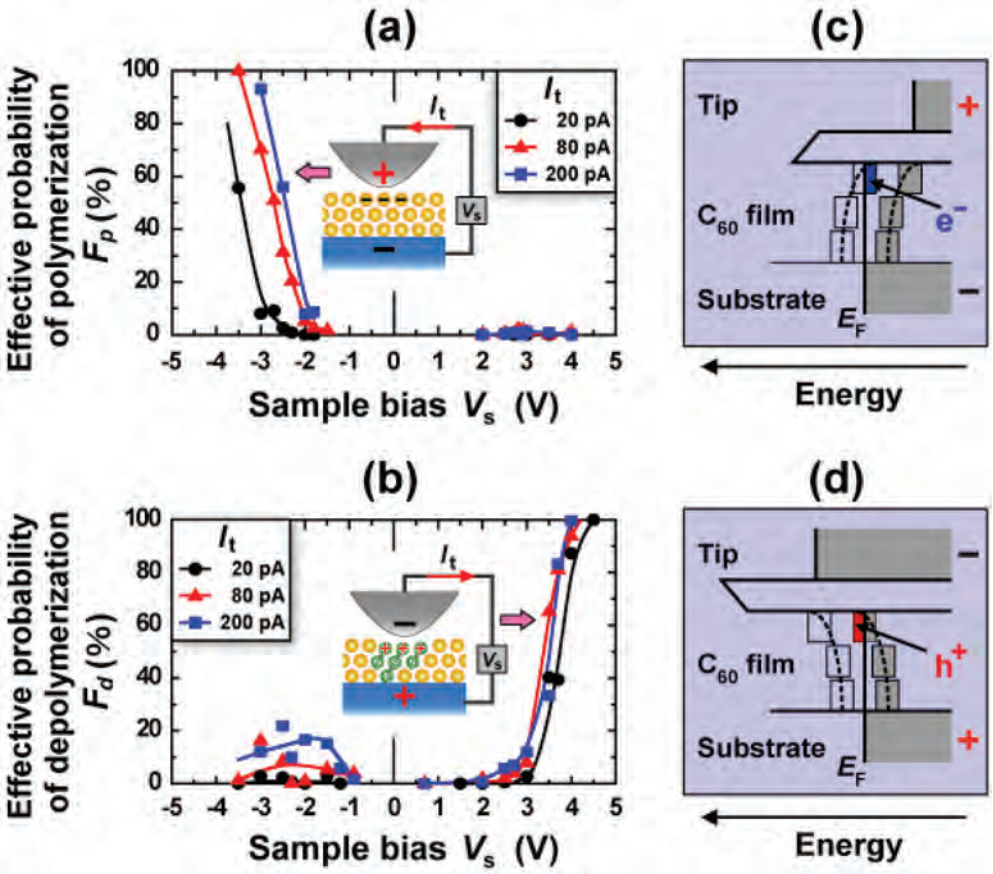

Figure 8. Effective probabilities of (a) Polymerization and (b) Depolymerization between C_{60} molecules induced by an STM tip in a C_{60} trilayer film [53]. The measurements were made as a function of sample bias V_s from about −4.0 to 4.5 V at different tunneling currents I_t = 20, 80, and 200 pA. Insets in (a) and (b) Schematically show that local C_{60} molecules are negatively and positively ionized due to an STM tip when negative and positive V_s's are applied, respectively. (c,d) Schematic potential energy diagrams of the whole experimental system consisting of the substrate, C_{60} trilayer film, vacuum gap, and STM tip when negative and positive V_s's were applied, respectively.

depolymerization has been shown to achieve 190 Tbits/inch^2 (T: Tera-; $\times 10^{12}$) which is higher by two orders of magnitude than that of the state-of-the-art HDD devices. Figure 9 shows bit operations at a single-molecule-level using a C_{60} trilayer film at RT. The STM-induced formation of C_{60} dimers/trimers is clearly observed as a depression (dark) area (Figure 9(b)). This is because C_{60} molecules at the outermost layer react with other C_{60} molecules in the underlying layers as illustrated in Figure 9(a). These facts indicate that not only writing/erasing digital bits but also readout of the recorded bits can be performed with the same STM tip (Figure 9(c)), thus being advantageous for realizing ultra-high density molecular memory devices. In addition, the nonvolatility of the recorded bits was confirmed to be more than 1 week [53]. Although the density of digital bits using STM-induced C_{60} polymerization/depolymerization is smaller than that using atomic-scale bit operation or DNA-based data storage technology, bit operations do not require low temperatures for single chlorine atoms on Cu(100) [71] or complicated and expensive procedures for DNA encoding and decoding [73].

When the STM-induced C_{60} polymerization/depolymerization technique is practically used for high-density data storage, there are several issues to be solved. From a viewpoint of storage speed, the speed of STM-induced polymerization/depolymerization must be at late comparable to that (10^6–10^8 bits/sec) of the present HDD. Currently, the storage speed was reached to 3.6×10^2 bits/s at fast [58], which is actually limited by a pulse width (a few ms) of the applied voltage to induce C_{60} polymerization/depolymerization. Further study is necessary to achieve data writing and erasing with a speed of ca. 10^6 bits/s for practical use by improving the quantum efficiency (η) of both polymerization ($\eta_p = 2 \times 10^{-7}$ reaction/hole) and depolymerization ($\eta_d = 3 \times 10^{-8}$ reaction/electron).

2.3.2. CO_2 immobilization

Immobilization and reuse of environmentally hazardous compounds such as CO_2, NO_x, or SO_x will play key roles in solving our environmental and energy issues [74,75]. One possible way is to use porous materials with nanospace [76]. Given that these nanoporous materials exhibit high electrical conductivity or high heat-resistance, electrochemical or heat

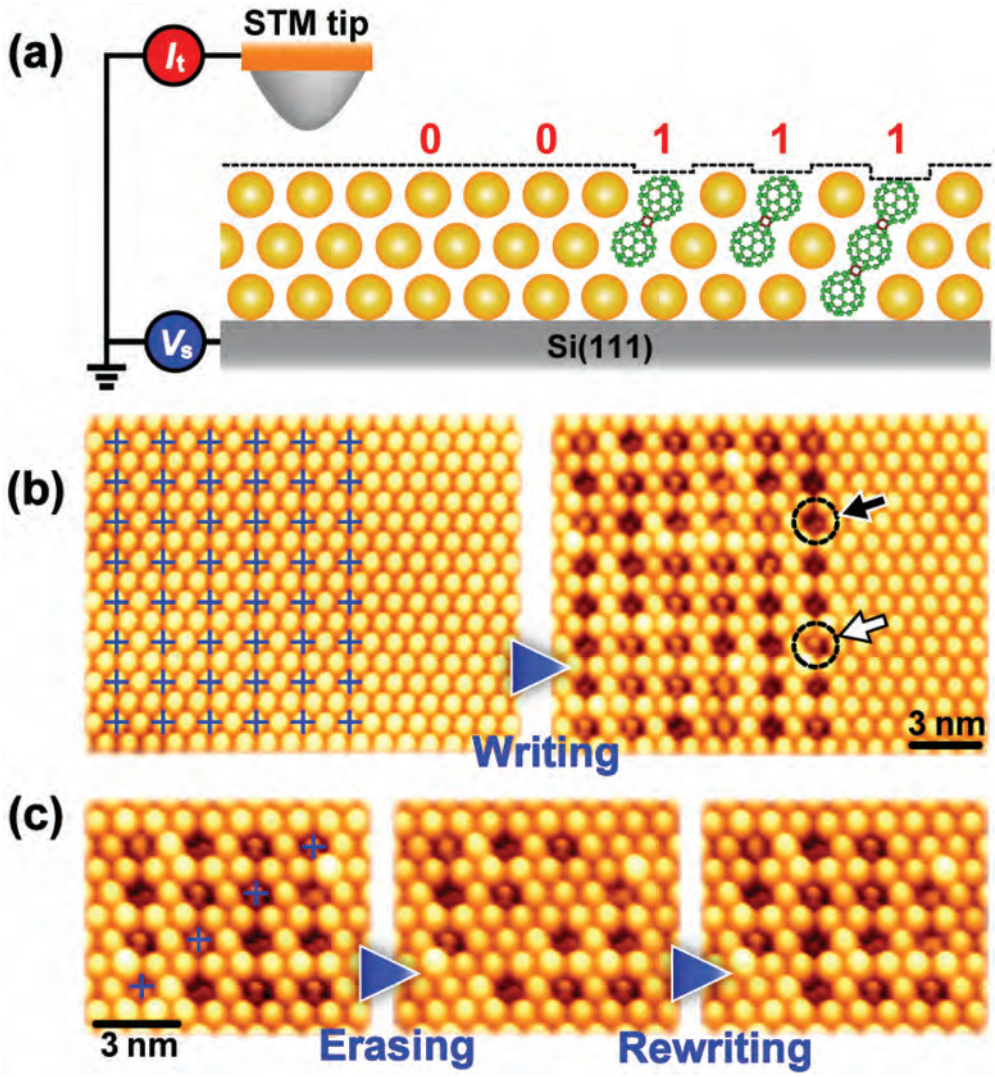

Figure 9. Ultrahigh-density data storage using C_{60} trilayer film as a recording media [53,58]. (a) Schematic side views of binary digital data ('0' and '1') stored in C_{60} film. (b) STM images observed before (left) and after (right) data writing. (c) STM images showing data erasing (left to central) and rewriting (central to right). All of data storage operation were carried out at RT.

treatments can be utilized to enhance chemical reactions in their nanospace.

As described in Sections *2.1* and *2.2*, the 1D peanut-shaped C_{60} polymer film has a HCP structure shown in Figure 3, which results in formation of sub-nm spaces with a size of ca. 0.3 nm and 0.6 nm periodically arranged (Figure 1 of Ref. [76]). In addition, the 1D polymer exhibits physical properties arising from 1D metal and a high heat-resistance at least up to 723 K. These findings suggest that the robust sub-nm space can act as a specific reaction field in a similar manner to those of conventional porous materials [74–81].

After the 1D peanut-shaped C_{60} polymer film was exposed to atmospheric air for 30 min at RT, Nakaya et al. examined the change in *in situ* infrared (IR) and mass spectra of the 1D C_{60} polymer under UHV conditions in combination with first-principles calculations based on DFT when compared to those of the pristine polymer (Figure 3 and 4 of Ref. [82]), and found that CO_2 is immobilized as a carbonate ion (CO_3^{2-}) in the sub-nm space of the 1D polymer film *via* [$CO_2 + H_2O$] reaction [51], despite the fact that the reaction [$CO_2 + H_2O$] is hard to proceed at RT in the gas phase (the activation energy, E_a = ca. 2 eV [83]). Although a pristine C_{60} film also has a similar sub-nm space inside, it was confirmed that no significant differences in their IR spectral features before and after atmospheric-air exposure are observed (Figure S2 in the supporting information of Ref. [82]). Thus, the 1D metallic peanut-shaped C_{60} polymer as a framework of the sub-nm space also plays a crucial role in promoting the reaction at RT.

To reveal the mechanisms behind the reaction occurred at RT in the sub-nm space, Kitagawa's group theoretically examined the most energetically preferable location of CO_2 molecule in the sub-nm space, using a sub-nm space model (Figure 10(a)). The electronic structure of the model obtained at the PM6 level of theory exhibited a weak charge polarization especially around the bridged concave portions (Figure S3a of Ref. [82]). Figure 10(b) shows the

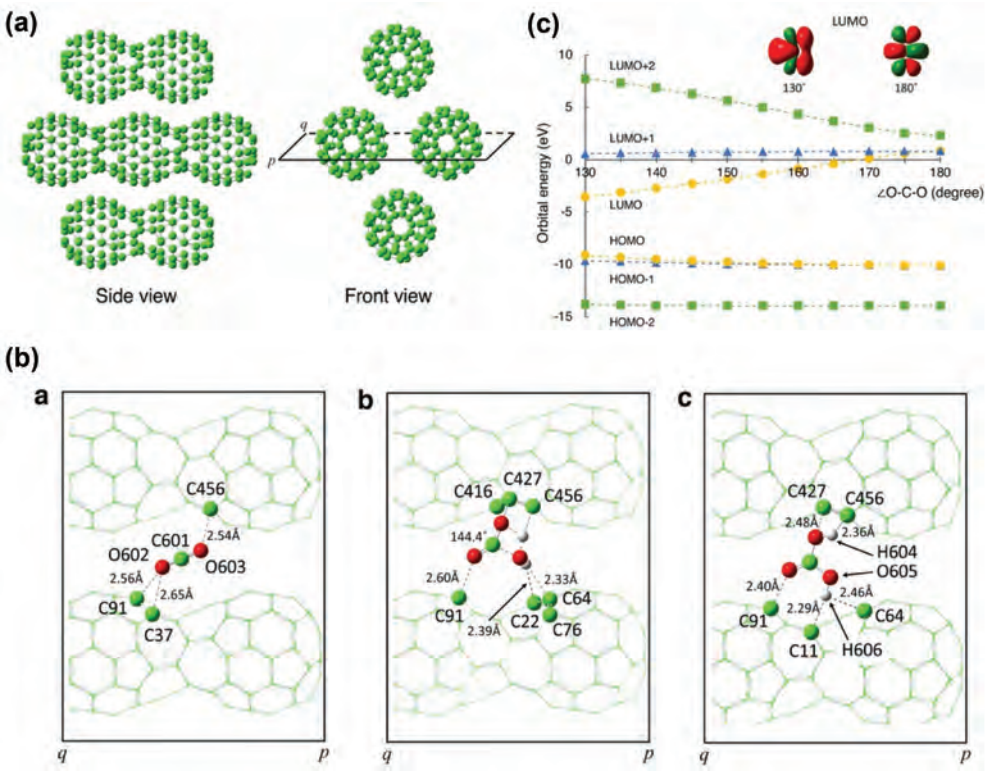

Figure 10. (a) Model structure of 1D peanuts-shaped C_{60} polymer film for quantum chemical calculations. (B) Optimized molecular structure of (a) CO_2, (b) transition state (TS) obtained at a lower convergence, and (c) H_2CO_3 in the sub-nm space. Symbols *p* and *q* correspond to those in the front views of Figure 5(a). The contacting carbon atoms and adsorbed molecules are shown as ball-models, and are connected by dashed lines together with their distances. (C) Change in the frontier orbital energies of CO_2 with respect to ∠O–C–O bond angle. At each angle, only the C–O bond distance was optimized. As the angle decreases, only the LUMO energy decreases monotonically and becomes negative below 170°, implying that the LUMO has an electron affinity [82]. Nakaya et al. [82]; licensed under a Creative Commons Attribution (CC BY) license.

optimized geometrical structure of the CO_2–H_2O transition state (TS) in the sub-nm space, whereas Figure 10(b) shows that of H_2CO_3 formed from the reaction. Only under a lower convergence condition, one TS was found along the reaction coordinate (Figure S4 in the supporting information of Ref. [82]), whereas they found product H_2CO_3 directly *via* no TSs under a higher convergence condition (Figure 10(b)). This suggests that the E_a of $[CO_2 + H_2O]$ reaction is very small or negligible in the sub-nm space of the 1D polymer film, which resembles a proton transfer process [84]. Figure 10(c) shows the dependence of valence molecular orbital (MO) energies on the ∠O-C-O bond angle. The lowest unoccupied MO (LUMO) energy was lowered monotonically to be a negative value at bond angles below 170°. This implies that the LUMO has an electron affinity. Furthermore, the insets show that a carbon pσ-type orbital of the LUMO expands more toward the obtuse-angle side of CO_2 at smaller ∠O-C-O angles. This suggests that the bending motion promotes $[CO_2 + H_2O]$ reaction from the obtuse-angle side, giving rise to a decrease in the E_a. Thus, factors such those mentioned above work together to promote the reaction at RT *via* no or negligible TSs. Alternative mechanisms were also discussed, but they can be excluded (Supporting information in Ref. [82]).

There have been many conventional methods to activate CO_2 radioactive-chemically, thermochemically, biochemically, photochemically, electrochemically, and catalytically [85]. The common idea among them is to add electrons to LUMO of CO_2, because the LUMO features an antibonding orbital. Thus, the reduction of CO_2 makes O=C=O bonding weakened to become reactive. On the other hand, in the nanospace of 1D peanut-shaped C_{60} polymer film, CO_2 is activated at RT *via* enhancement in its angular vibration by CO_2 molecule pinning due to local Coulomb interactions, which reduces the LUMO energy to be negative (electron affinity emerges).

The CO_2 uptake performance of the 1D C_{60} polymer film is estimated to be 1.60 mmol/g, which is comparable to that of zeolites such as Li-LSX (1.34 mmol/g) and Na-LSX (0.87 mmol/g) obtained under the similar exposure conditions (in 1 atm air at RT) [86].

2.3.3. 1D N-doped peanut-shaped C_{60} polymer

To mitigate the greenhouse effects, considerable efforts have been made to convert CO_2 to valuable industrial chemicals. The widely used catalysts for CO_2 reduction are metals [87], metal oxides [88],

metal chalcogenides [89] and metal – organic complexes [90]. However, these metal-containing catalysts are costly and their energy efficiency is limited. Peanut-shaped carbon nanotubes (PSNTs) are of particular interest because of their exotic geometry with a large specific surface area and with positive and negative Gaussian curvatures respectively with negative and positive polarizations. Thus, PSNTs are expected to have good performance for CO_2 capture and conversion [91,92].

As shown in Figure 5, there are many types of 1D PSNTs studied theoretically, and FP5N was found to be energetically stable with a high symmetry and to exhibit a metallic feature [41], which share the structural features of C_{60} cages and 1D uneven peanut-shaped structures. Figure 11 shows the geometric structure of front (a) and side (b, d) views for FP5N, along with the electronic band structure and DOS (c). There exist 5-, 6- and 8-membered rings where the C atoms have much more complicated bonding environments that offer more flexibility to tune the reactivity when compared to conventional 1D CNTs. This enables us to improve the catalytic performance. Figure 11(c) shows that FP5N is metallic as the partially occupied bands cross the E_F. When one nitrogen (N) atom is substitutionally doped into the C-framework of FP5N, there are four chemically nonequivalent doping sites (α, β, γ, and δ shown in Figure 11(b)).

The total energy calculations for the four N-doped FP5N configurations were carried out to determine the most preferred doping site. The configuration with N at γ site was found to be most stable, which is lower in energy by 0.04, 0.07 and 0.17 eV than the configurations with N at α, β and δ sites, respectively. Then, Wang et al. calculated the band structure of the most stable structure of N-doped FP5N.

Figure 12(a) reveals that the metallic feature still remains after N doping at *γ* site. When more N atoms are substitutionally doped into FP5N, the possible N doping sites were categorized into three different types: pyridinic N (in the hexagonal ring), pyrrolic N (in the pentagonal ring), and octatomic N (in the octatomic ring), as shown in Figure 12(d). Each of these sites is unique in the N-doped FP5N structure. The preferred electrocatalyst candidates were screened by calculating the free energy changes for both •COOH and •OCHO radicals at all the catalytic sites in the first proton-coupled electron transfer (PCET) step [93]. The free energy change of •COOH adsorption was found to be much smaller than that of •OCHO. This suggests that the first intermediate PCET step for CO_2 electrocatalytic reduction (CO_2ER) is •COOH. The geometrical structure of •COOH adsorbed on top of the C atom near the graphitic N is shown in Figure 12(b) (front view) and (c) (side view).

Figure 13 shows (a) the free energy diagram for the lowest energy pathway of CO_2 converted to CO or CH_3OH by including the zero-point energy, vibrational entropy and solvent correction, and (b) the corresponding intermediate configurations. It is found that the pristine FP5N has the highest free energy barrier for the first step of CO_2 adsorption,

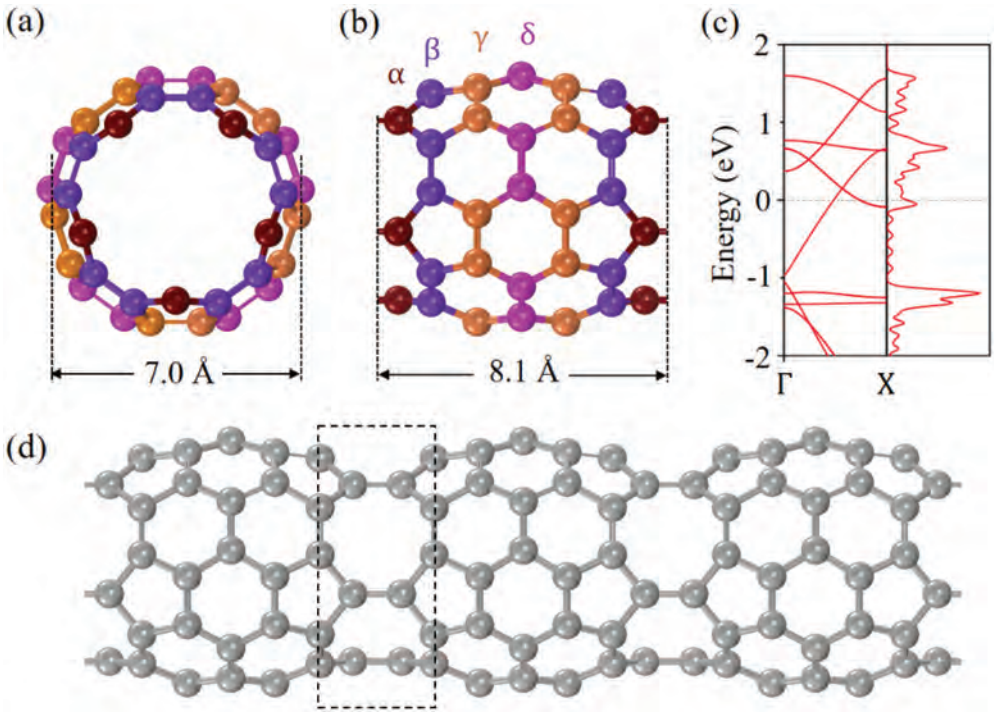

Figure 11. (a) Front and (b) Side view of FP5N. (c) Electronic band structure and DOS of FP5N. (d) Side view of a 1 × 1 × 3 supercell of FP5N [92]. Reprinted with permission from Zhou et al. [92]. Copyright 2019 Elsevier.

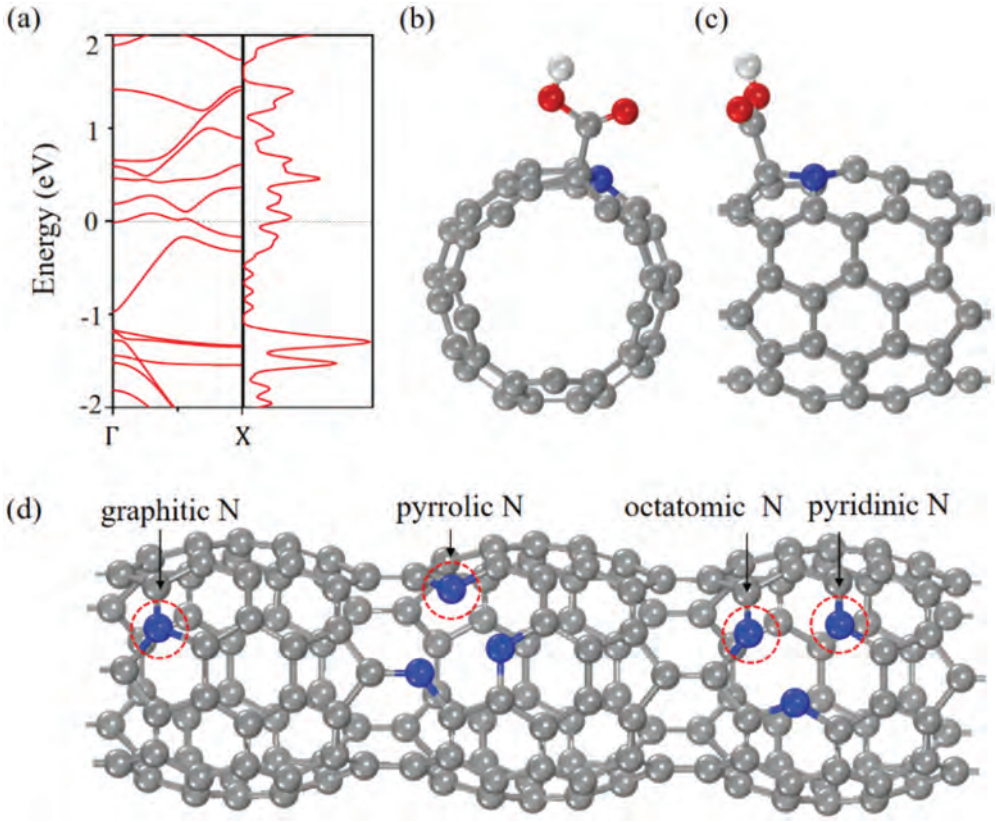

Figure 12. (a) Electronic band structure and DOS of N-doped FP5N structure. (b) Front and (c) Side view of •COOH adsorbed on N-doped FP5N. (d) Schematic diagram of different N doping catalytic sites on FP5N [92]. Reprinted with permission from Zhou et al. [92]. Copyright 2019 Elsevier.

which hinders CO_2 conversion. The potential-limiting step [•COOH → •CO] for graphitic N is 0.65 eV, and •CO prefers to decompose to CO rather than getting further hydrogenated because of the much more negative free energy change of [•CO → CO (g)] reaction. Even though the energy change (0.65 eV) for the graphitic N is larger than that of the pyrrolic N (0.52 eV), pyridinic N (0.52 eV) and octatomic N (0.60 eV), it still lowers the overpotential by 0.92 V as compared to that in the pristine FP5N, which produces CO at a higher overpotential of 1.57 V. This significantly improves CO_2 conversion performance by N doping. Furthermore, since the binding energy of •COOH to the graphitic N (2.67 eV) is higher than that of the pristine FP5N (1.58 eV), •COOH binds more strongly on the graphitic N.

During the CO_2 conversion, the first electron transferred to the chemically stable CO_2 usually possesses a high overpotential. On the contrary, in the case of FP5N, the free energy changes of [CO_2 → •COOH] reaction for pyrrolic N, octatomic N and pyridinic N are estimated to be only 0.04, −0.01 and 0.06 eV, respectively. These free energy changes are rather small in contrast to the pristine FP5N (1.57 eV), the graphitic N (0.48 eV) and many more promising electrocatalysts including transition metal Cu (0.41 eV). The binding energies of •COOH to pyrrolic N, octatomic N and pyridinic N are estimated to be 3.12, 3.17 and 3.10 eV, respectively, which are all higher than that of graphitic N. This is because pyrrolic N, pyridinic N and octatomic N are electron-rich, which bind CO_2 while electrons of graphitic N are located in the π^* antibonding orbital, making them less accessible for CO_2 binding. The strong binding of CO_2 to pyrrolic N, pyridinic N and octatomic N sites accounts for the small free energy change for the first step: [CO_2 → •COOH]. The free energy changes of [•CO → CO (g)] reaction at pyrrolic N, octatomic N and pyridinic N are all larger than that of [•CO → •CHO] reaction. This indicates that •CO is likely to produce •CHO rather than CO gas and further hydrogenated.

The potential-limiting steps for pyrrolic N, octatomic N, and pyridinic N are found to be [•H_2COH → CH_3OH (g)], [•CHO → •HCOH], and [•CO → •CHO] reactions, respectively. The corresponding overpotentials of CO_2 conversion are estimated to be 0.52, 0.52 and 0.60 V, respectively, which makes the whole reaction being spontaneous and exergonic. For octatomic N, the CO_2 conversion pathways are identified to be as shown in Figure 13(b) (front view).

$$CO2(g) \rightarrow \bullet COOH \rightarrow \bullet CO \rightarrow \bullet CHO \rightarrow \bullet HCOH \rightarrow \bullet H2COH \rightarrow CH3OH(l),$$

Since the large free energy change of [•CO → CO (g)] reaction makes •CO further hydrogenated, the final

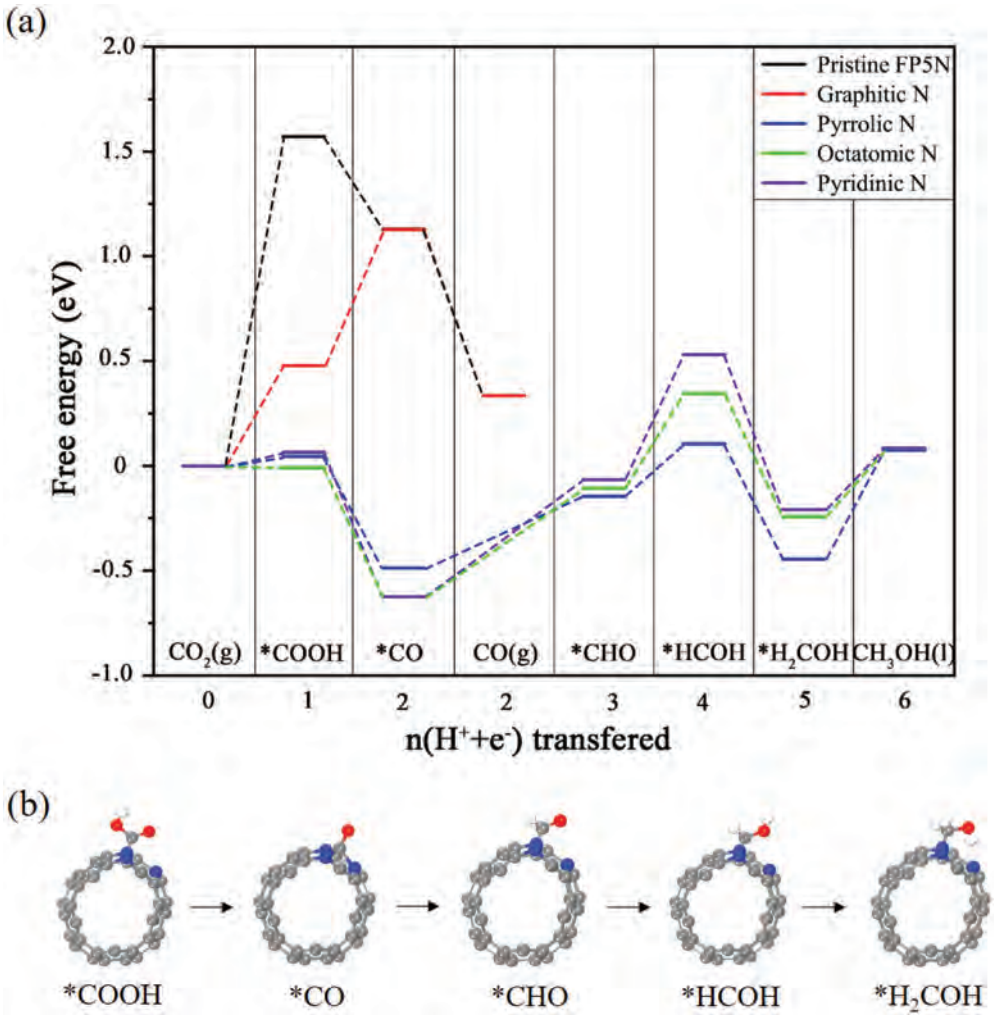

Figure 13. (a) Free energy diagrams of different catalytic sites for pristine and N-doped FP5Ns. (b) Configurations for the intermediates of •COOH, •CO, •CHO, •HCOH, and •H_2COH for CO_2ER on the octatomic N [92]. Reprinted with permission from Zhou et al. [92]. Copyright 2019 Elsevier.

product is CH_3OH for pyrrolic N, octatomic N and pyridinic N. This is rare for all kinds of N-doped carbon nanomaterials as catalysts for CO_2 conversion. When compared to metal catalysts, the N-doped PSNTs also have some merits. For instance, the overpotential of Mo-Bi bimetallic chalcogenide for reducing CO_2 into CH_3OH is 0.7 V [94], and among the metal electrocatalysts studied previously, copper is the only metal that is capable of reducing CO_2 to significant amounts of hydrocarbons and oxygenates with high overpotentials (0.9–1.1 V) [95,96], which is higher than that of N-doped PSNT. Thus, this finding demonstrates that the N-doped PSNT is a promising candidate to replace metal catalysts for effective CO_2 reduction.

In addition, it is also important to note that PSNTs possess much lower lattice thermal conductivity as compared to conventional carbon nanotubes (CNTs) besides the high performance for CO_2 immobilization and conversion. By using non-equilibrium molecular dynamics simulations and lattice dynamics together with DFT, Sun et al. found that the thermal conductivity of the PSNT is reduced by more than 90% as compared to that of CNTs and remains almost the same when different strains applied [97,98]. This exhibits very different behaviors from those of CNTs (the thermal conductivity decreases monotonically with increasing strain). The insensitive response of thermal conductivity against strain is due to the insensitivity of its phonon DOS and group velocity against strain. Furthermore, when 5–8 membered defect is introduced to PSNT, the lattice thermal conductivity of PSNT with the defect is less by one-tenth than that of pristine CNT with a similar radius. This arises from the low phonon group velocity, short relaxation time, large lattice vibrational mismatch and strong anharmonicity [97]. These findings provide new insight for 1D PSNT going beyond conventional CNTs.

3. Two-dimensional dumbbell-shaped C_{60} polymers and related nanocarbons formed *via* photo-induced polymerization

3.1. Structures

Since the first report on C_{60} polymerization by Ar-ion laser or UV-vis lamp irradiation of a pristine C_{60} film

at RT [70] by Rao et al., Onoe et al. investigated the structure of photopolymerized C_{60} films using *in situ* FT-IR spectroscopy [16], *in situ* x-ray photoelectron spectroscopy (XPS) [17,18], and *in situ* STM [20,49] under UHV conditions. The results of FT-IR, XPS, and STM found that C_{60} molecules are polymerized to form 1D/2D C_{60} polymer with a cross-linkage of [2 + 2] cycloadditional four-membered ring.

Figure 14 shows (a) the dependence of the IR intensity ratio (I_{2D}/I_{dimer}) on photo-irradiation time for 100 nm- (red) and 200 nm-thick (black) C_{60} films on cesium iodide (CsI) substrates, (b) schematic model for the spatial distribution of the dimer (blue) and 2D polymer (red) in each film, and (c) STM image of 100-h photo-irradiated C_{60} thin film formed on the Si(111)/∏3×∏3-Ag substrate. Figure 14(a) shows that the IR intensity ratio of the 200 nm-thick C_{60} film (blue) increased remarkably until 100-h irradiation and became saturated after 150-h irradiation, whereas that of the 100 nm-thick C_{60} film (red) increased remarkably until 200-h irradiation and is extrapolated to be saturated after 500-h irradiation. It is found that the saturated (I_{2D}/I_{dimer}) value of ca. 1.15 for the 100 nm-thick film was larger than that of ca. 0.8 for the 200 nm-thick film. This difference can be well explained by assuming that the 2D dumbbell-shaped C_{60} polymer is formed within a few surface layers, as shown in Figure 14(b). This assumption is strongly supported by the results obtained using XPS (photoelectrons were measured from a few nm in depth of the film) [17,18]. In addition, it was observed from the result in Figure 14(c) that the 2D [2 + 2] dumbbell-shaped C_{60} polymer is formed on the outermost C_{60} layer. Furthermore, even if the film thickness increases, the formation region of the 2D polymer from the outermost layer should remain unchanged as long as the same photo-irradiation time. Thus, the saturated (I_{2D}/I_{dimer}) value of the 100 nm-thick film was greater than that of the 200 nm-thick one.

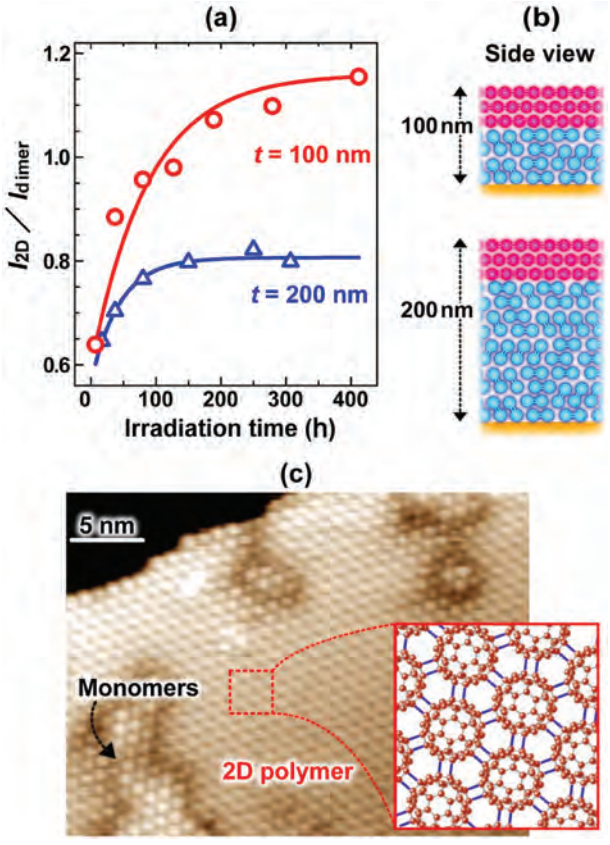

Figure 14. (a) The dependence of the intensity ratio (I_{2D}/I_d) on photo-irradiation time for 100 nm- (red) and 200 nm-thick (black) C_{60} films on CsI, (b) Schematic model for the distribution of the dimer (blue) and 2D polymer (red) in each film, and (c) STM image of 100-h photo- irradiated C_{60} multi-layers formed on Si(111)/√3×√3-ag substrate [20]. Onoe et al. [20]; licensed under a Creative Commons Attribution (CC BY) license.

For practical use of the 2D dumbbell-shaped C_{60} polymer, it is important to consider its heat resistance. Unlike the 1D peanut-shaped C_{60} polymer film, the [2 + 2] four-membered ring was drastically dissociated at temperatures exceeding 373 K with an activation energy of 1.25 eV [69]. Accordingly, the 2D C_{60} polymer is limited to be used for devices that not only work below 373 K but also are fabricated in all processes below the temperature.

More recently, semiconducting monolayer 2D C_{60} networks (band gap: ca. 1.6 eV) *via* cross-linking of C–C single and [2 + 2] cycloaddition bonds have been reported to be synthesized by Hou et al. and indicated no thermal decomposition after heating at 600 K for 10 min [99]. However, since the decomposition of the 2D polymer proceeds on the basis of the kinetics with some activation energy as heating time becomes long, the heating condition thus examined is too short to confirm the heat resistance of the 2D monolayer C_{60} networks. Accordingly, it is further necessary to investigate the heating-time dependence of the 2D network decomposition. Section 3.3.2 will discuss the kinetics of thermal decomposition of a photopolymerized C_{60} film with [2 + 2] cycloaddition bonds.

3.2. Fundamental properties

Onoe and Nakayama et al. examined the electrical properties of the 2D C_{60} photopolymer using four-probe measurement [19]. Although Okada and Saito theoretically predicted the 2D polymer to be a semiconductor with a band gap smaller by one-third [100] than that (1.85 ± 0.04 eV) for pristine C_{60} solids [101], no attempts to examine the electrical properties of the 2D C_{60} photopolymer have been made until then.

Figure 15 shows the *I*–*V* characteristics and sheet resistance of photopolymerized C_{60} film (after 400 h UV-vis irradiation) obtained in atmospheric air at RT. Here, the red circles represent the *I*–*V* characteristics measured using probes 1 and 4 (outer probes),

whereas the blue squares represent the sheet resistance derived from voltages measured by probes 2 and 3 (inner probes), as shown in the inset. The sheet resistance and *I*–*V* characteristics of a pristine C_{60} film could not be obtained, because its sheet resistance was beyond the range of the measurement system at that time. This was presumably due to oxygen in air which is well known to act as an electron capture (O_2 is well known to become O_2^- as a superoxide radical). Judging from the inset of the optical micrograph taken during the corresponding four-probe measurements, the 2D dumbbell-shaped C_{60} polymer film seems to be uniformly smooth and to have no grain boundaries within the measurement area. The typical inter-probe distance was set in the range of 8–40 μm, ensuring an appropriate film thickness for the four-probe measurements. When the inter-probe distance (L = 8–40 μm) is much larger than the film thickness (t = 70 nm), the sheet resistance (R_s) of the film can be evaluated in terms of $R_s = 4.532 \times (V/I)$, and the resistivity (ρ) can be calculated from $\rho = R_s \times t$. Here, V is the difference in voltage between the two inner probes, and I is the current flow between the two outer probes.

As shown in Figure 15, the *I*–*V* curve demonstrates that the 2D C_{60} polymer is a non-doped semiconductor (except during the plateau of the *I* – *V* curve). Since the R_s depends on the current flow between the two outer probes, the resistance thus obtained does not correspond to the carrier density of the 2D C_{60} polymer film. The carriers in the film are apparently supplied by the biased metal probe during the measurements. Namely, the 2D C_{60} polymer has no carriers (electrons or holes) contributing to the conductivity at RT. This makes it difficult to estimate the resistivity of the polymer using the four-probe measurement system at that time. In addition, although the temperature dependence of R_s should be measured for the 2D C_{60} polymer in order to determine the energy gap of the film from Arrhenius plot, the experimental system resulted in temperature variations only from RT to ca. 373 K, which were insufficient to estimate the energy gap. However, considering that R_s and *I*–*V* characteristics of the pristine C_{60} film could not be obtained using the measurement system, these results nonetheless demonstrate that the 2D photopolymer is a semiconductor, which is consistent with the theoretical prediction [100]. According to first-principles calculations of C_{120} dumbbell-shaped dimer (Figure 4 of Ref. [19]), it is clear that nodes where no electrons exist are formed at the [2 + 2] four-membered ring between adjacent C_{60} molecules for the HOMO. This indicates that electrons cannot move from one C_{60} to another without excitation-induced hopping. In other words, there is some energy gap for the electron hopping between adjacent C_{60} molecules *via* the ring. Consequently, the 2D dumbbell-shaped C_{60} polymer has a semiconducting property. On the other hand, electrons can move over the whole dumbbell dimer for the LUMO, indicating that the 2D C_{60} polymer exhibits conducting properties when electrons are excited from the HOMO to the LUMO.

For a further study, we will examine the temperature dependence of R_s for the 2D C_{60} polymer film using *in situ* UHV four-probe measurement apparatus equipped with a helium cryostat [102,103].

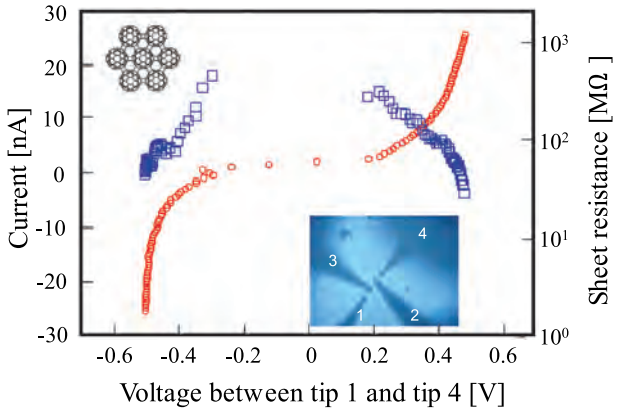

Figure 15. Sheet resistance (blue square) and current – voltage curve (red circle) of the photopolymerized C_{60} film using four-probe measurements in air at RT. Inset shows the optical micrographs obtained during the measurements. A typical distance between adjacent probes was set in the range of 8–30 μm [19]. Onoe et al. [19]; licensed under a Creative Commons Attribution (CC BY) license.

3.3. Potential applications

3.3.1. Organic solar cells

Since C_{60} has a large electron affinity of 2.68 eV [104], C_{60} is often used an electron acceptor for organic solar cells (OSCs) that expects to be one of the wearable power generators. After photogenerated excitons are separated to electron/hole carriers at a donor/acceptor interface, the electrons diffuse to a cathode through the C_{60} film. However, since the resistivity of pristine C_{60} film is very high (2×10^6 Ωcm [43]) even under UHV conditions, it is one of the main factors to lower the energy conversion efficiency of OSCs. As described in the previous section, photopolymerized C_{60} film exhibits a semiconducting property with the LUMO where electrons can move from one to another *via* the [2 + 2] bond between adjacent C_{60} molecules (Figure 4 of Ref. [19]).

From this standpoint, Kato et al. [13] investigated the modification of the structural and optical properties of C_{60} film used as an acceptor in terms of photopolymerization between adjacent C_{60} molecules in order to improve the external quantum efficiency (*EQE*) of Zinc phthalocyanine (ZnPc)/C_{60} OSC. Figure 16 shows (a) the *EQE* of [ITO/ZnPc/P-C_{60}/Al] (red) and [ITO/ZnPc/C_{60}/Al] (green) OPV cells (Inset

schematically illustrates the OPV cell structures), and (b) UV-vis-NIR spectra in a wavelength region of 400–900 nm. As shown in Figure 16(a), the *EQE* increased in a wavelength region both of 400–480 nm and of 520–580 nm for photopolymerized C_{60} film (named as p-C_{60} film) used instead of the pristine one, which well corresponds to the increase in the absorbance of p-C_{60} film in both the wavelength regions as shown in Figure 16(b). In addition, since the structure of ZnPc film used as a donor remained unchanged after 37-h photo-irradiation (Figure 3 of Ref. [13]), its optical characteristic is considered to be unchanged. In fact, they confirmed no changes in UV-vis-NIR spectra of 40 nm-thick ZnPc film even after 74-h UV-vis photo-irradiation (photon energy: 2–4 eV, fluence: 0.4 W cm^{-2}), as shown in Figure S1 of Ref. [11]. Consequently, the increase in *EQE* in those wavelength regions is mainly due to an increase in the number of photogenerated intra- and inter-molecular excitons in p-C_{60} film [105,106]. Details of discussion on the other structural and physical properties of C_{60} film influenced by photo-irradiation have been described in Ref. [11].

3.3.2. Organic thermoelectric materials

C_{60} films exhibit a giant Seebeck coefficient (S) of more than 150 mV K^{-1} (at 300 K) [107] and a lower thermal conductivity (k) of 0.4 W m^{-1} K^{-1} (at 300 K) [108] when compared to those (S = 0.27 mV K^{-1}, k = 1.6 W m^{-1} K^{-1} at 300 K) of Bi_2Te_3 commercially available [109], thus being expected to be one of powerful candidates for next-generation wearable power generator used to wearable devices (sensors, etc.). However, the electrical conductivity (σ) of C_{60} films was reported to be an order of 10^{-5} Ω^{-1} cm^{-1} [44], which is quite smaller than that (307 Ω^{-1} cm^{-1}) of Bi_2Te_3 [109]. According to the figure of merits ($Z = S^2\sigma k^{-1}$) used as a performance index, it is necessary to increase the σ of C_{60} films drastically while suppressing the decrease in the S for practical use, because there is the trade-off relationship between S and σ (the Mott's formula) [110]. For instance, a typical way to increase the σ of C_{60} films is to use dopants such as alkali metals (potassium: K) [44,111] and organic di-metal complexes [112] into the films. However, while the σ was increased with a fraction of the complexes in the film, the S was comparably decreased.

One possible way to solve this issue is to utilize C_{60} photopolymerization, because a part of polymerization in C_{60} films contribute to increase the σ while suppressing the decrease in the S. Actually, the polymerization reduces their intermolecular distance by ca. 10% *via* the [2 + 2] four-membered ring, thus increasing the σ [19,20]. This idea is quite similar to that of the carrier energy filtering effects [113,114]. This inversely consider that a perfect C_{60} polymer network *via* the [2 + 2] four-membered ring is randomly broken to suppress a phonon-mediated thermal conductivity. When C_{60} molecules are polymerized, the absorption band of C_{60} films correspondingly becomes broadened toward a longer wavelength [13]. Accordingly, the modification of the electrical and optical properties by photopolymerization is useful to improve the device performance such as OSCs, as shown in Figure 16.

Thus, the control of the proportions of individual C_{60} photopolymers is expected to further modify the physicochemical properties of C_{60} films for the device performance. To the best of our knowledge, there have been no reports to discuss the proportion distribution for C_{60} monomer, dimer, trimer and larger oligomers kinetically so far, though Metelov et al. reported on depolymerization of C_{60} dimer [115] and two-dimensional (2D) rhombohedral C_{60} polymer [116] synthesized by the HPHT method.

Izumi et al. studied the kinetics of photopolymerization and depolymerization in C_{60} films using *in situ* Fourier-transform infrared spectroscopy for the development of C_{60}-based thermoelectric materials [117]. Figure 17 shows (a) the irradiation-time dependence of individual proportions of C_{60} monomer (x_1: blue), $(C_{60})_2$ dimer (x_2: red), and $(C_{60})_n$ (n ≧ 3) oligomers (x_n: green), (b) the annealing-temperature dependence

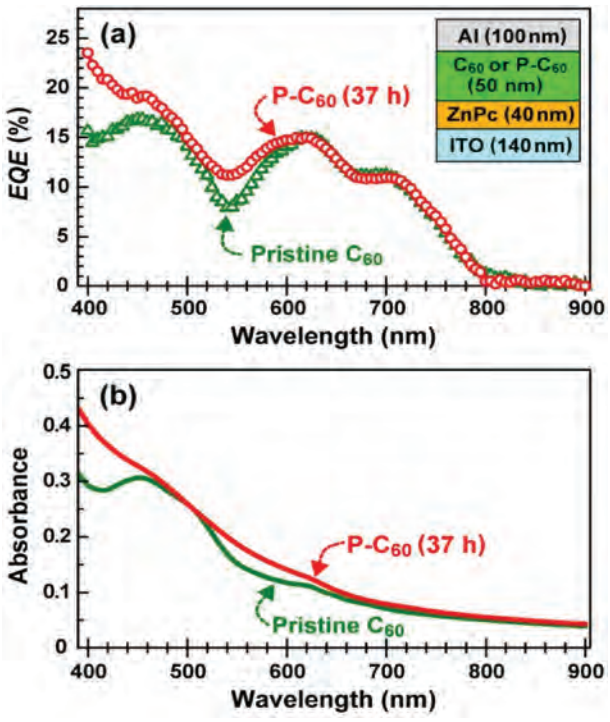

Figure 16. (a) *EQE* spectra of [ITO (140 nm thick)/ZnPc (40 nm thick)/C_{60} (50 nm thick)/Al (100 nm thick)] (green), and [[ITO (140 nm thick)/ZnPc (40 nm thick)/P-C_{60} (50 nm thick)/Al (100 nm thick)] (red) OPV cells, and (b) UV-vis-NIR spectra of pristine (green) and photopolymerized (red) C_{60} films in a wavelength region of 400–900 nm [13]. Kato et al. [13]; licensed under a Creative Commons Attribution (CC BY) license.

of those proportions, (c, d) the Arrhenius plots for rate constants k_2 [$(C_{60})_2 \rightarrow 2\ C_{60}$] and k_3 [$(C_{60})_3 \rightarrow (C_{60})_2 + C_{60}$], and (e) the annealing-time dependence of x_1 (blue), x_2 (red), and x_3 (green) at 110°C [117]. As shown in Figure 17(a), the proportion of the monomer (x_1), dimer (x_2), and oligomers (x_3) was saturated to be 4%, 72%, and 24%, respectively, after 40 h irradiation of ultraviolet light (fluence: 0.2 W cm^{-2}, wavelength: 300–410 nm). This indicates that the polymerization between adjacent $(C_{60})_2$ dimers is very difficult to occur. In other words, to increase the proportions of $(C_{60})_n$ oligomers, [$C_{60} + (C_{60})_{n-1}$] reaction should be proceeded.

They further examined the decomposition kinetics, and it is interesting to note from Figure 17(b) that x_2 (the dimer) decreases at temperatures exceeding 100°C, whereas x_3 (the oligomers) remains constant up to 140°C. Correspondingly, the E_a of decomposition for $(C_{60})_2$ dimer and $(C_{60})_n$ (n ≧ 3) oligomers was obtained to be 1.26 eV and 1.78 eV from the Arrhenius plots of k_2 (c) and k_3 (d), respectively. Details of discussion on the reason behind the E_a of the trimers larger than that of the dimer have been described in Ref. [117]. Accordingly, one given annealing temperature in the range of 100–140°C makes it possible to proceed the decomposition of $(C_{60})_2$ dimer with remaining the proportion of $(C_{60})_n$ (n ≧ 3) oligomers unchanged. Figure 17(e) shows the results of x_1, x_2, and x_3 at an annealing temperature of 110°C. The proportion of the $(C_{60})_2$ dimer (x_2) becomes smaller than that of the $(C_{60})_3$ trimers (x_3) after more than 300 h. Thereafter, further photoirradiation will induce the polymerization of [$C_{60} + (C_{60})_{n-1}$ ($n > 3$) → $(C_{60})_n$] to increase the x_n value. Therefore, the iterations of [photopolymerization/110°C-thermal decomposition] cycle can control the proportion of $(C_{60})_n$ oligomers to modify the physicochemical properties of photopolymerized C_{60} films for application to C_{60}-based thermoelectric materials, as shown in Figure 18.

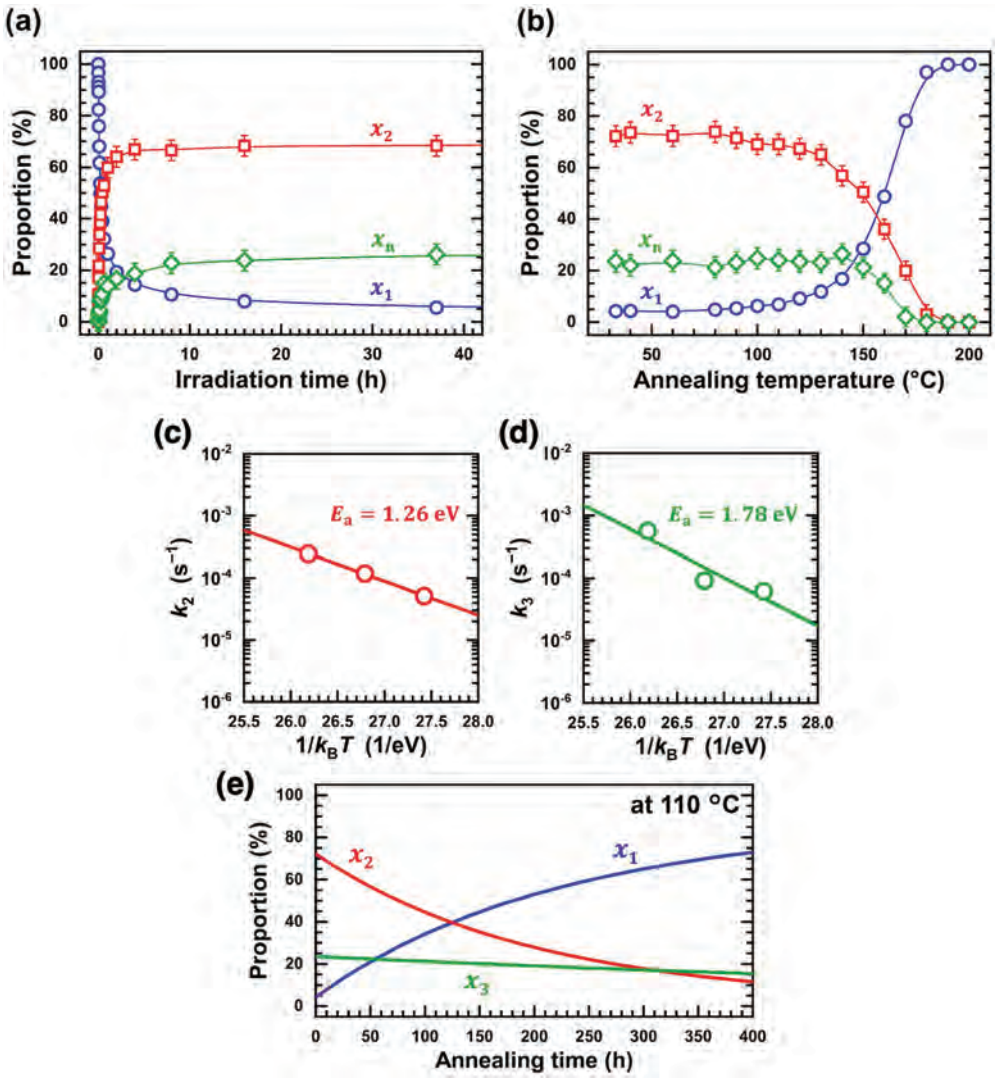

Figure 17. (a) Irradiation-time dependence of individual proportions of C_{60} monomer (x_1: blue), dimer (x_2: red), and trimers/oligomers (x_n: green), (b) Annealing-temperature dependence of x_1 (blue), x_2 (red), and x_n (green), (c, d) The Arrhenius plots for k_2 and k_3, and (e) The annealing-time dependence of x_1 (blue), x_2 (red), and x_3 (green) at 110°C [117]. Izumi et al. [117]; licensed under a Creative Commons Attribution (CC BY) license.

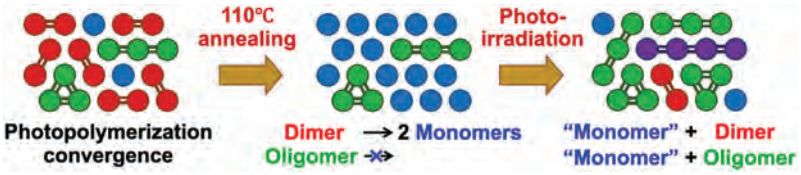

Figure 18. Schematic illustration for controlling the proportion of $(C_{60})_n$ oligomers *via* the iterations of [photopolymerization/110°C-thermal decomposition] cycle.

Actually, Nakaya et al. obtained that the power factor ($PF = S^2\sigma$), which is one of the important indexes for thermoelectric device performance, of C_{60} film after 8 h UV-vis photoirradiation ($PF = 2.3 \times 10^{-5}$ W m^{-1} K^{-2}) became greater by one order than that (2.3×10^{-6} W m^{-1} K^{-2}) of pristine C_{60} film [118]. Considering that *PF* of more than 10^{-3} W m^{-1} K^{-2} is enough for practical use, the [photopolymerization/110°C-thermal decomposition] cycle is a useful way to improve the *PF* of the photopolymerized C_{60} film.

4. Other low-dimensional nanocarbons

4.1. C_{60} peapods

C_{60} peapods can be regarded as composite materials in which C_{60} molecules are encapsulated within the internal cavities of CNTs (Figure 19(a)), which was first reported in TEM images (Figure 19(b)) of C_{60} molecules aligned in a single-walled CNT (SWCNT) that was accidentally observed by Smith et al. [119]. However, the C_{60} peapods now can be synthesized conveniently with a well reproducibility by using sublimation of C_{60} (dry process) or 'nano-extraction' (wet process) technique [120] in the presence of CNTs with open-ended tips. The arrangement of the encapsulated C_{60} molecules can be controlled utilizing the diameter of CNTs used as a container. In particular, when using SWCNTs with a diameter of 1.4 nm, C_{60} molecules with a diameter of 0.7 nm can efficiently achieve van der Waals contact within the internal space of SWCNTs. This results in formation of an ideal 1D C_{60} array (Figure 19(b)).

The distinctive structure of C_{60} peapods has attracted considerable attention from the perspectives of physics and engineering. Especially, their electronic structures, optical, electrical, and magnetic properties have been extensively investigated so far [121]. The impracticality of extracting the 1D C_{60} molecules from the peapods has been focused to examine the properties of C_{60} peapods treated as a C_{60}/CNT composite nanocarbon.

Notably, the interactions between CNTs and C_{60} are utilized to control the properties of the CNTs. For instance, the strong electron affinity of C_{60} [105] causes electron transfer from SWCNTs to C_{60} molecules, resulting in a partial positive charge distribution

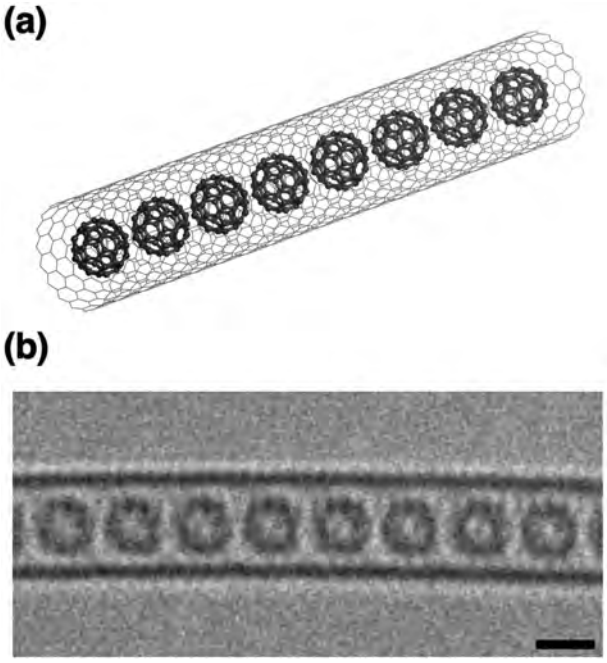

Figure 19. Structure of fullerene peapods: (a) Molecular model of C_{60} molecules encapsulated in (18,0) single-walled CNT, (b) Aberration-corrected TEM image of C_{60} fullerene peapods. Here, the black scale bar is 1 nm.

along the axis of SWCNTs. This makes SWCNTs featured as a p-type material. For example, Roth's group demonstrated a single-electron transistor using C_{60} peapods [122]. In addition, this property has also been reported to enhance a field emission efficiency [123]. Furthermore, the dependence of C_{60} filling ratio on the thermal conductivity of C_{60} peapods has been investigated by equilibrium molecular dynamics (MD) simulations and obtained that the maximum thermal conductivity of C_{60} peapod at filling ratio of 50% is greater by ca. 30 times than that of pristine CNT [124].

In a similar manner to C_{60}, C_{70} [125], higher-order fullerene molecules [126], nitrogen-doped fullerenes (N@C59) [127], and metallofullerenes [128] were reported to form 1D arrays as well. Recently, 1D $DySc_2N@C_{80}$ array in CNTs exhibited a single-molecule magnet [129].

Attempts to produce 1D C_{60} polymers *via* polymerization between the adjacent encapsulated C_{60} molecules in the peapods have been extensively made since the material's discovery [119]. Fusion induced by EB irradiation was confirmed in the first report [119], and

it was shown that fusion reactions between C_{60} molecules progress upon 100 kV EB irradiation, eventually converting the internal 1D C_{60} array in SWCNT to form double-walled carbon nanotubes (DWCNTs). DWCNTs can also be formed from C_{60} peapods under heat treatment at 1200°C [130]. This method is useful to synthesize DWCNTs with precisely controlled diameters at a bulk scale. Another way to polymerize C_{60} in peapods is chemical doping, which emerges a metallic property of the peapods [131].

When C_{60} peapods are considered as a starting material for the synthesis of 1D C_{60} polymers, CNTs can be used as a test tube in order to track the polymerization reaction of C_{60} using HRTEM [132]. In particular, the development of spherical aberration correctors and high-speed imaging detectors has improved the resolution and frame rates of TEM significantly. This leads to investigate the structure and kinetics of reactions between C_{60} molecules precisely at atomic scale. Nakamura and Harano et al. recorded TEM video with a millisecond time-resolution to capture EB-induced fusion reaction from two C_{60} molecules to one coalesced C_{120} and identified several metastable C_{120} intermediate species based on their shapes and sizes [133]. These reactions occur stochastically, and the lifetime of individual intermediate species varies correspondingly (Figure 20(a)). From the statistical analysis of numerous recorded images of cascade reactions, the average lifetime of various intermediate species was determined. High-energy short-lived intermediate species such as P02 were successfully observed as shown in Figure 20(b). Moreover, by examining both the frequency of individual reaction events in various temperature ranges and the temperature dependence of the reaction rates, it is possible to estimate the E_a from the excited states [134]. This revealed that the fusion reaction causes *via* the excited states of C_{60} and C_{120} intermediate species that depend on EB kinetic energy [135].

4.2. Wavy-structured graphenes

Noda et al. theoretically examined wavy-structured graphenes as new metallic carbon allotropes using first-principles calculations based on DFT [136]. Although an ideal graphene is exactly a 2D flat layer atomically, the wavy-structured graphene has convex and concave curved structures induced by the topological defects consisting of 5- and 7-/8-membered rings, respectively. Figure 21(a) shows schematic illustration of the wavy-structured graphene with the defects, which consists of sixty C atoms per unit cell. Such the wavy-structured graphene can be formed from graphene by introducing topological defects *via* the GSW transformation [137,138]. Thus, we examined the effects of the topological defect consisting of pentagon-octagon-pentagon membered rings (named Mickey-Mouse-shaped defect) on the wavy-structured graphene.

Unlike the 2D flat graphene which exhibits strongly dispersive bands intersecting at the Dirac point near E_F, the band structure of the wavy-structured graphene with the Mickey-Mouse-shaped defects shows simultaneous occurrence of both flat and dispersive bands, which are parts of an anisotropic Dirac cone tilted from the isotropic one of the pristine graphene (see Figure 21(b)). Owing to the presence of the flat bands, the wavy-structured graphene has an extremely high DOS near E_F, which is quite similar to that of high-performance metal catalysts such as platinum and palladium [139–141]. As far as we examined, similar characteristics of the flat band and high DOS near E_F have been found for the other wavy-structured graphene models (see Supplementary Information of Ref. [136]).

4.3. Penta-nanotubes

It is well known that CNTs can be obtained from graphene, namely (n, m) nanotube can be defined using a chiral vector, $C_{nm} = n\boldsymbol{a_1} + m\boldsymbol{a_2}$. Here, $\boldsymbol{a_1}$ and $\boldsymbol{a_2}$ are the unit vectors, and n and m are the integers to indicate the number of unit vectors in graphene. Due to the gapless semi-metallic feature of graphene, the electronic properties of CNTs exhibit a high chirality-dependence. Namely, a CNT is metallic only when its C_{nm} satisfies $(n-m) = 3l$, where l is an integer. The difficulty in fabricating and separating CNTs with certain conductance (metallic or semiconducting) greatly hinders its application in nanoelectronics.

Going beyond the conventional graphene, penta-graphene exclusively consisting of only 5-membered rings was proposed by Wang et al. [142], which exhibits many interesting properties due to its unique geometric structure (negative Poisson's ratio, intrinsic piezoelectricity, giant out-of-plane, and second harmonic generation susceptibility) [143,144]. In similar, penta-nanotubes can be constructed by rolling up the penta-graphene sheet along the (n, m) chiral vectors with n=m ranging from 2 to 8, as shown in Figure 22(a) [142]. The optimized geometry of a (3, 3) penta-tube is presented in Figure 22(b). Figure 22(c,d) shows the dynamic and thermal stabilities of this penta-nanotube obtained using phonon spectra calculations and *Ab initio* MD (AIMD) simulations, respectively. All the (n, n) penta-nanotubes are dynamically robust as well as thermally stable up to 1000 K.

More interestingly, the penta-nanotubes inherit the semiconducting feature of penta-graphene. As shown in Figure 23, they are all semiconducting with medium size energy band gaps from 2.008 to 2.731 eV [145]. When the diameter of the inner layer increases from 5.69 Å in (4, 4) to 12.10 Å in (8, 8), the band gap decreases rapidly

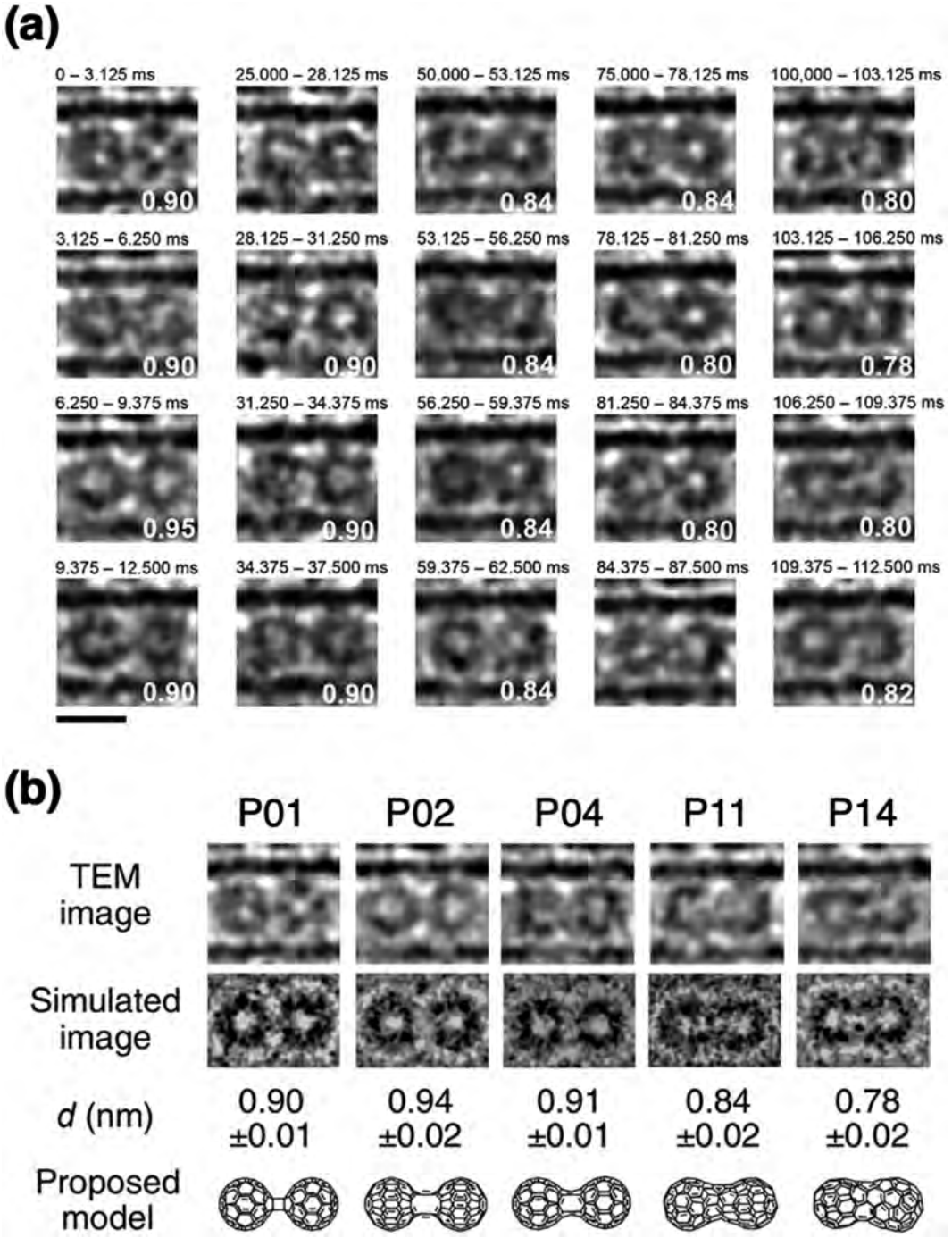

Figure 20. Millisecond-scale TEM video imaging of multistep conversion of C_{60} peapods under electron-beam irradiation [133]: (a) Cinematographic frames (3.125 ms/frame) of a C_{60} dimer undergoing generalized Stone-Wales transformation. The time begins with the start of recording, and the numbers on the right bottom are the intermolecular distances in nm. The scale bar is 1 nm. (b) Experimental, simulated images and proposed models of coalesced dimers for observed intermediates in TEM. Reprinted with permission from Shimizu et al. [133]. Copyright 2022 American Chemical Society.

with increasing the diameter. When the inner diameter is larger than 20.22 Å in (13, 13), the bad gap becomes insensitive to the inner diameter due to the small curvature effects for large penta-nanotubes. This is very different from the conventional CNTs with a chirality-dependent conductance. Namely, they can be metallic or semiconducting that depends on their chirality. This unique feature of penta-nanotube demonstrates the advantages for application to nano electronic devices. In addition, the band gap can be effectively tuned by strain (Figure 23(b) for (9,9) nanotube), where the bad gap reduces linearly under pressive strain, while increasing nonlinearly with stretch.

Mechanically, the elastic modulus of penta-nanotubes was reported to be up to 1000 GPa [146–149], which is comparable to that of conventional CNTs [150]. In addition, several other exceptional features such as the auxeticity at ambient conditions, the ultimate tensile stress of 85–110 GPa, and the critical strain up to 25%

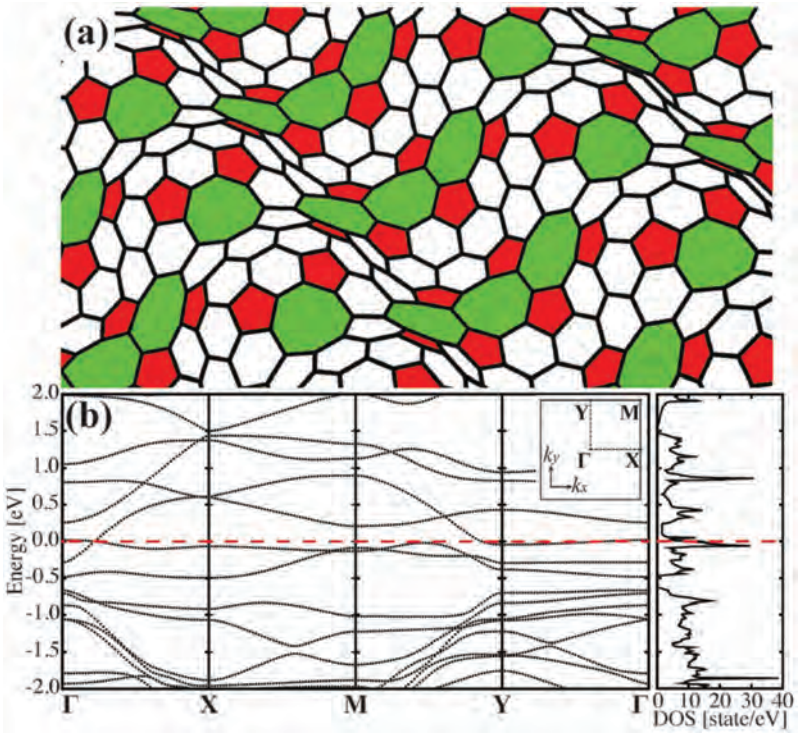

Figure 21. (a) Geometrical structure and (b) Band structure along Γ–X–M–Y–Γ directions and DOS of the wavy-structured graphene with Mickey-Mouse-shaped defects that are periodically aligned parallel to the *y*-direction. The inset in (b) shows the Brillouin zone of the wavy-structured graphene, where fractional coordinates at Γ, X, M, and Y points are given by (k_x, k_y) = (0.00, 0.00), (0.50, 0.00), (0.50, 0.50), and (0.00, 0.50), respectively. A tilted Dirac cone is located between Γ and X points at the Fermi level. Horizontal dashed red lines in the band structure and DOS indicate the Fermi level [136]. Reprinted with permission from Noda et al. [136]. Copyright 2014 the Royal Society of Chemistry.

have confirmed the mechanical superiority of penta-nanotubes [146,151] over conventional CNTs.

In contrast to the feature of the bandgap, the fracture patterns of penta-nanotubes strongly depend on the chirality of the nanotubes. For example, Sousa et al. [148] showed that the armchair-type penta-nanotubes are suddenly fractured at lower tensile strain values due to the differences in bonding alignments when compared to zigzag-type penta-nanotubes. Interestingly, penta-nanotubes can have direct α-phase and inverted β-phase, which depend on the inner dimers being parallel or perpendicular to the main axis of the tube [152]. In addition, strain engineering can be used to improve the structural performance of penta-nanotubes and to enhance their electronic and mechanical tunability under applied conditions. For instance, Wang et al. found that the compressive strain can drive a transition from semiconductor to metal in β-phase (4, 4), (5, 5), and (6, 6) tubes [152]. Sousa et al. [146] showed that (11,11) β-phase penta-nanotube experiences a structural transition to (11,11) α-phase under tensile stretching at RT. In addition, elasticity – plasticity transition can also be induced by tensile strain engineering [149].

Using large-scale MD simulations, Chen et al. [149] found that penta-tube has comparable mechanical properties with that of the conventional CNTs. However, unlike the brittle CNTs, penta-tube exhibits a large extensibility (with failure strain exceeding 60%) and behaves plastically during tensile deformation. The plasticity is inherently caused by the phase transition from pentagonal to polygonal (including trigonal, tetragonal, hexagonal, heptagonal, and octagonal) carbon rings. The plastic feature of penta-tubes depends intrinsically on the tube-diameter and strain-rate.

Recently, Shah et al. [153] reported that porous carbon penta-nanotubes can be used as a sensor for halogen gas (F_2, Cl_2, Br_2, I_2), where the host carbon atoms were selectively removed to create the nanopores on the tube surface, and the I – V curves suggested the performance of gas detection. Furthermore, interaction energy graphs showed the efficient separation of various halogen molecules by functionalizing the pores with F_2, Cl_2 and H atoms.

Besides the penta-nanotubes formed from penta-graphene, the other penta-tubes have also been studied. For example, based on the experimental synthesis of penta-$PdSe_2$ sheet, Kuklin et al. [154] found that the electronic properties of (n, 0) penta-$PdSe_2$ tubes, like that of the penta-$PdSe_2$ monolayer, are semiconducting with similar band gaps, whereas (n, n) tubes exhibit indirect – direct band gap transitions following the increase in the tube diameter. Motivated by the recent synthesis of penta-NiN_2 sheet, Ati et al. [155] explored the H_2 adsorption on (n, 0) penta-NiN_2

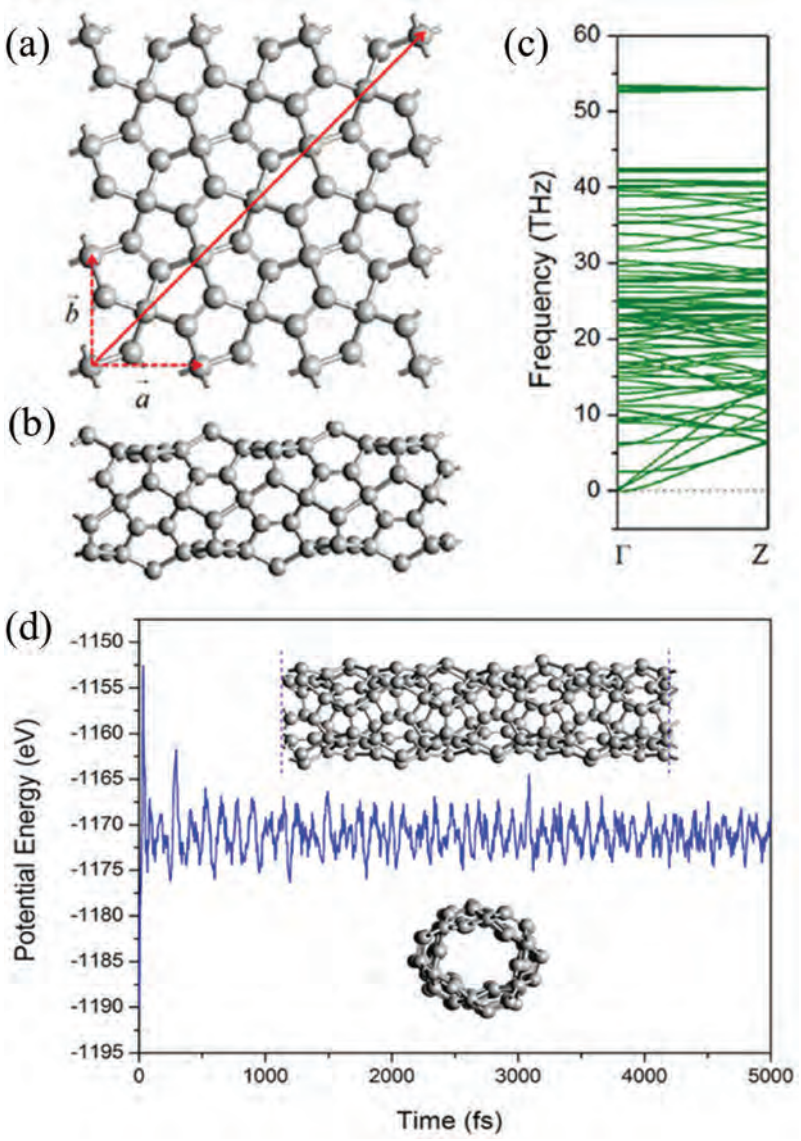

Figure 22. (a) Illustration of chiral vectors of penta-tube. Dashed lines with arrows denote the lattice basis vector. (b) Side view of the optimized structure of (3, 3) penta-tube, (c) The corresponding phonon spectrum, and (d) evolution of potential energy of (3, 3) penta-tube during AIMD simulations at 1000 K, where the insets show snapshots of atomic configuration at the end of the simulation [142].

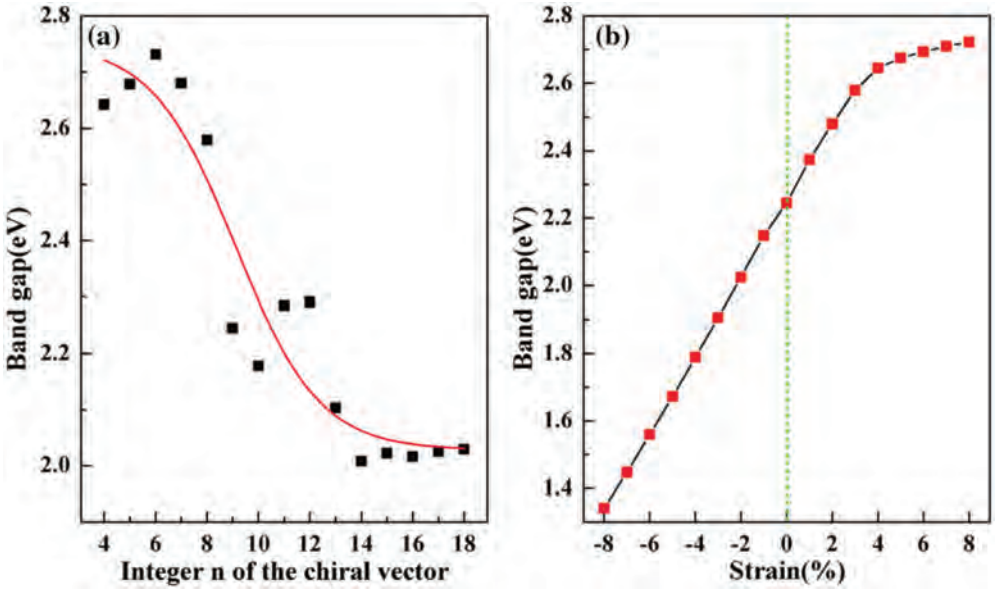

Figure 23. (a) Band gap changing with diameter for (n, n) penta-nanotubes, (b) Strain modulated band gap of (9,9) penta-nanotube [145]. Reprinted with permission from Wang et al. [145]. Copyright 2020 Springer.

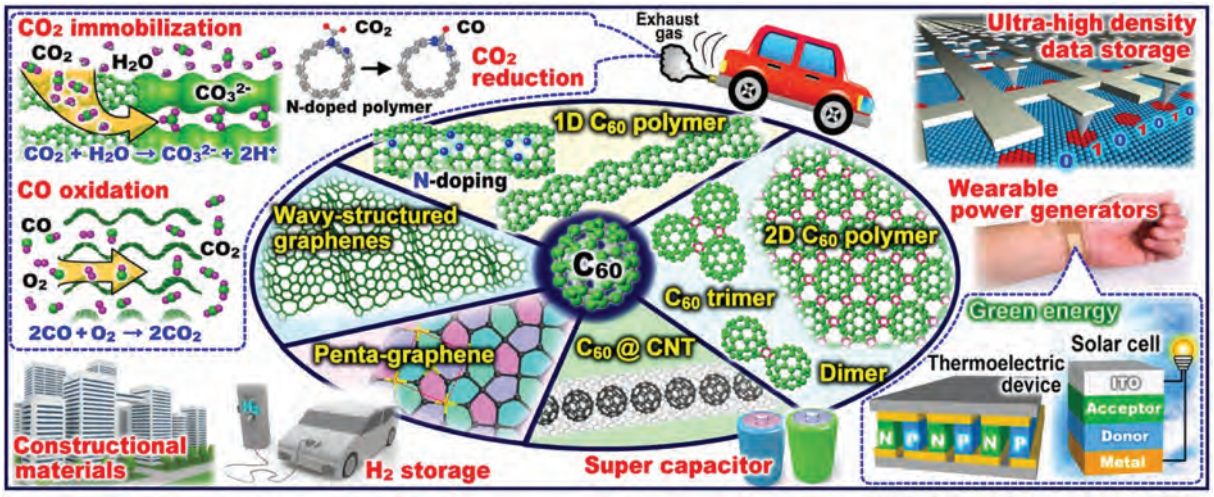

Figure 24. Schematic illustration of C_{60}-based low-dimensional nanocarbons in this review: structures and potential applications based on their fundamental properties.

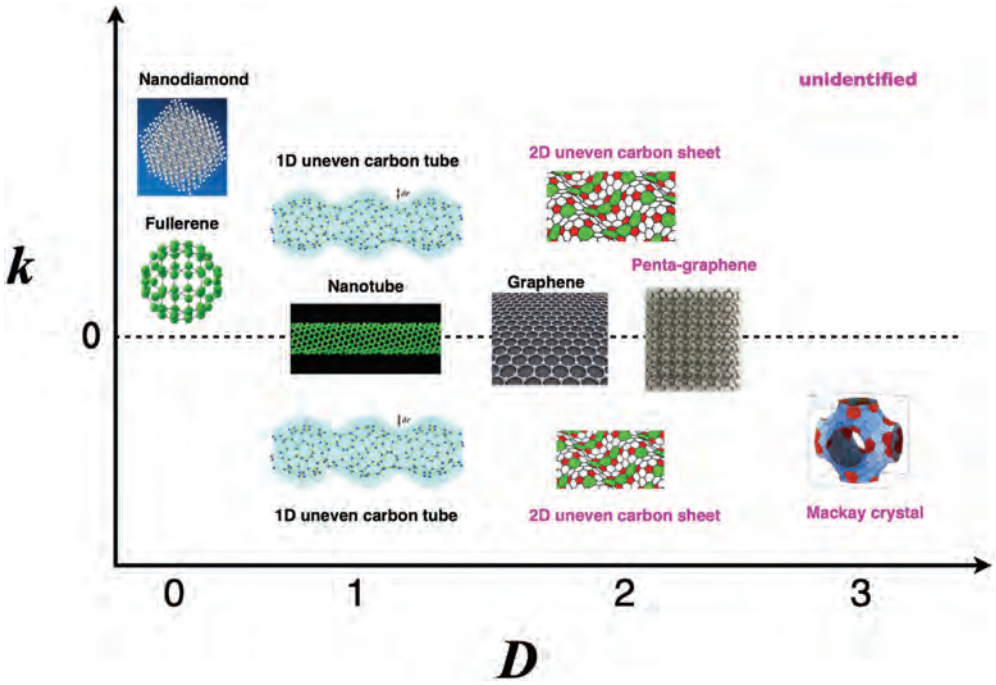

Figure 25. Schematic mapping of low dimensional nanocarbons with respect to Gaussian curvature (*k*) and dimension (*D*), along with 3D Mackay crystal.

tubes, and found that when the sheet is curved into nanotubes, the Ni-N distance is enlarged due to the stress, which weakens the orbital hybridizations between Ni and N, and reduces the charge transfer from Ni to N. The Ni ion with a less charge on the tube shows a weak polarizing ability for H_2 molecule.

The studies on penta-nanotubes have significantly expanded the family of 1D carbon nanomaterials with new features and provided more options for device applications.

5. Outlook

This review has focused on the structures, fundamental properties, and potential applications of low-dimensional C_{60} polymers and related nanocarbons formed *via* photo- and electron-induced polymerization and those of other low-dimensional nanocarbons such as C_{60} peapods, wavy-structured graphenes, and penta-nanotubes, as shown in the summary of Figure 24.

As described in Section 2.2, the 1D peanut-shaped C_{60} polymer is the only one material that can examine the properties in curved quantum systems experimentally. This is of great significance to cultivate a new interdisciplinary field between geometry and materials science by pioneering the unexplored doctrine of curved quantum systems (quantum mechanics of submanifolds). More recently, discrete geometry analysis has been applied to several 1D peanut-shaped C_{60} polymers

for exploring the correlation between mathematical and physical quantities [156]. Figure 25 shows the mapping of low-dimensional nanocarbons with respect to Gaussian curvature (k) and dimension (D), along with negatively curved graphitic 3D carbon crystals proposed by Mackay, Terrones, and the other groups [157–159]. Interestingly, Park et al. theoretically predicted to exhibit magnetism due to trivalent carbon radicals in the tetrapod core with a concave surface (Figure 1 of Ref. [160]). As shown in Figure 25, a flexibility of bond direction by sp^2–sp^3 combinations further discovers new novel carbon materials different from fullerenes, nanotubes, and graphene.

In our materials world that has hitherto been composed of two axes: physics and chemistry, novel materials have been discovered by 'knowledge', 'experience', and 'intuition' (for example, fullerenes, nanotubes, and graphene) so far. This is so-called 'Serendipity'. If modern mathematics is incorporated into the materials world as a new axis, novel materials discovered without 'Serendipity' (Beyond Serendipity) will no longer be a dream (Figure 3.21 of Ref. [15]).

Disclosure statement

The authors declare no potential conflict of interest.

Funding

A part of results was financially supported by a special coordination fund of the Science and Technology Agency of the Japanese Government, the Precursory Research for Embryonic Science and Technology (PRESTO) and the Program of Core Research for Evolutional Science and Technology (CREST) of Japan Science and Technology Agency (JST), New Energy and Industrial Technology Development Organization (NEDO) (Grant No. 16101402-0), Grants-in-Aid for Scientific Research (KAKENHI) (Grant No. 21200032, 14J00217, 17H03384, 18H01826, 21H01758, 23H04874) of Japan Society for the Promotion of Science (JSPS), Iketani Science and Technology Foundation, Leading Project of the Ministry of Education, Culture, Sports, Science and Technology (MEXT), and the WPI program (MANA) of MEXT.

Notes on contributors

Jun Onoe was graduated from Osaka University (master degree) in 1987 and worked for Panasonic Co. Ltd at the same year. He moved to RIKEN in 1990 and got Ph.D. from Kyoto University in 1997. Thereafter, he moved to Tokyo Institute of Technology as an associate professor in 2002, and has been a professor at Nagoya University since 2014. The current topics of his concern are 1) an interdisciplinary between modern geometry and materials science, 2) organic solar cells and thermoelectric devices, and 3) nano-space materials applied to the disposal of nuclear wastes and the recycling of precious metals.

Yusuke Noda earned Ph.D. from Yokohama National University in 2015. After joined MI^2I project at NIMS in 2016 as a postdoctoral researcher, He move to Nagoya University in 2018 as a specially appointed assistant professor. He moved to Kanazawa Gakuin University in 2020 as a lecturer, and thereafter to Okayama Prefectural University as an associate professor in 2021, and has been an associate professor at Kyushu Institute of Technology in 2024. His research interests are 1) computational materials science for semiconductors applied to electronic devices, 2) machine-learning for defects in semiconductors, and 3) machine-learning predicting physical properties of semiconductors.

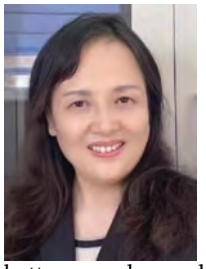

Qian Wang earned a PhD degree from Tohoku University (Japan) in 2001 and has been a full Professor at Peking University since 2011. Her current research interests include computational design and theoretical study of carbon-based materials and pentagon-based functional materials for spintronics, thermoelectricity, piezoelectricity, battery anodes, and heterojunctions.

Koji Harano got a Ph.D. from The University of Tokyo in 2007. After postdoctoral work at Tohoku University, he became an Assistant Professor at the Department of Chemistry in The University of Tokyo in 2007. In 2015, he was appointed as a Project Associate Professor of Molecular Technology Innovation Presidential Endowed Chair Laboratory at The University of Tokyo. In 2022, he moved to NIMS as Principal Researcher in Electron Microscopy Group. His current research interests are the development of new electron microscopic techniques for imaging of self-assembled materials and their application to construction of functional materials.

Masato Nakaya was graduated and received a master degree from Fukui University in 2002 and received a Ph.D. from Osaka University in 2010. He worked for National Institute for Materials Science (NIMS) during 2002–2011 as a research associate. After that, he joined Japan Science and Technology Agency (JST) as a postdoctoral researcher in 2012. He has been an associate professor at Nagoya University in 2014. One of his research targets is realization of practical energy-harvesting devices using nanomaterials such as functional molecules, nanocarbons, and nanospace materials using scanning probe microscopes and laboratory-made microprobe systems.

Tomonobu Nakayama received a master's degree from Tokyo Institute of Technology (1988) and later received a Ph.D. from the University of Tokyo (1999). After working for a private company, JRDC (former JST) and RIKEN as a research scientist, he joined NIMS in 2002. He is specialized in nanoscale science and technology, especially in atom/molecule manipulations using scanning probe microscopes, electrical characterization at nanoscale, and recently very much interested in neuromorphic materials integration for brain-like information processing. He received Commendation for Science and Technology by MEXT, Commendation for Fellow of Japan Society of Applied Physics, and so on.

References

[1] Kroto HW, Heath JR, O'Brien SC, et al. C_{60}: Buckminsterfullerene. Nature. 1985;318 (6042):162–163. doi: 10.1038/318162a0

[2] Iijima S. Helical microtubules of graphitic carbon. Nature. 1991;354(6348):56–58. doi: 10.1038/354056a0

[3] Novoselov KS, Geim AK, Morozov SV, et al. Electric field effect in atomically thin carbon films. Science. 2004;306(5696):666–669. doi: 10.1126/science.1102896

[4] Dresselhaus MS, Dresselhaus G, Eklund PC. Science of fullerenes and carbon nanotubes. New York: Academic Press; 1995. and references therein.

[5] Jorio A, Dresselhaus MS, Dresselhaus G, editors. Carbon nanotubes. Berlin: Springer; 2008. and references therein.

[6] Wu YH, Yu T, Shen ZX. Two-dimensional carbon nanostructures: fundamental properties, synthesis, characterization, and potential applications. J Appl Phys. 2010;108(7):071301. doi: 10.1063/1.3460809

[7] Ueno H, Osawa S, Osawa E, et al. Stone-wales rearrangement pathways from the hinge-opened [2+2] C_{60} dimer to IPR C_{120} fullerenes: vibrational analysis of intermediates. Fullerene Sci Technol. 1998;6 (2):319–338. doi: 10.1080/10641229809350204

[8] Takashima A, Onoe J, Nishii T. *In situ* infrared spectroscopic and density-functional studies on the cross-linked structure of one-dimensional C_{60} polymer. J Appl Phys. 2010;108(3):033514. doi: 10.1063/1.3462446

[9] Frisch MJ, Trucks GW, Schlegel HB, et al. Gaussian 03, revision B.05. Pittsburgh (PA): Gaussian, Inc.; 2003.

[10] Iwasa Y, Arima T, Fleming RM, et al. New phases of C_{60} synthesized at high pressure. Science. 1994;264 (5165):1570–1572. doi: 10.1126/science.264.5165.1570

[11] Pekker S, Jánossy A, Mihaly L, et al. Single-crystalline $(KC_{60})_n$: a conducting linear alkali fulleride polymer. Science. 1994;265(5175):1077–1078. doi: 10.1126/science.265.5175.1077

[12] Wang G-W, Komatsu K, Murata Y, et al. Synthesis and X-ray structure of dumb-bell-shaped C_{120}. Nature. 1997;387(6633):583–586. doi: 10.1038/42439

[13] Kato M, Nakaya M, Watanabe S, et al. Photopolymerization effects on the external quantum efficiency of fullerene/zinc phthalocyanine heterojunction solar cells. AIP Adv. 2021;11 (7):075227. doi: 10.1063/5.0052714

[14] Onoe J, Nakayama T, Nakao A, et al. Clusters and nanomaterials. Kawazoe Y, Kondow T, Ohno K, editors. Heidelberg: Springer-Verlag; 2001. p. 135–169.

[15] Shima H, Onoe J. The role of topology in materials. Gupta S, Saxena A, editors. Chap. 3. Cham: Springer; 2018. pp. 53–84.

[16] Onoe J, Takeuchi K. *In situ* high-resolution infrared spectroscopy of a photopolymerized C_{60} film. Phys Rev B. 1996;54(9):6167–6171. doi: 10.1103/PhysRevB.54.6167

[17] Onoe J, Nakao A, Takeuchi K. XPS study of a photopolymerized C_{60} film. Phys Rev B. 1997;55 (15):10051–10056. doi: 10.1103/PhysRevB.55.10051

[18] Onoe J, Takeuchi K. How many [2+2] four-membered rings are formed on a C_{60} molecule when photopolymerization is saturated? Phys Rev Lett. 1997;79(16):2987–2989. doi: 10.1103/PhysRevLett.79.2987

[19] Onoe J, Nakayama T, Aono M, et al. Electrical properties of a two-dimensionally hexagonal C_{60} photopolymer. J Appl Phys. 2004;96(1):443–445. doi: 10.1063/1.1745121

[20] Onoe J, Nakaya M, Watanabe S, et al. Electron-beam-irradiation of photopolymerized C_{60} film studied using *in situ* scanning tunneling microscope, *in situ* Fourier-transform infrared spectroscopy, and first-principles calculations. AIP Adv. 2020;10 (8):085212. doi: 10.1063/5.0018985

[21] Onoe J, Nakayama T, Aono M, et al. Structural and electrical properties of an electron-beam irradiated C_{60} film. Appl Phys Lett. 2003;82(4):595–597. doi: 10.1063/1.1542943

[22] Onoe J, Ito T, Kimura S, et al. Valence electronic structure of cross-linked C_{60} polymers: *in situ* high-resolution photoelectron spectroscopic and density-functional studies. Phys Rev B. 2007;75 (23):233410. doi: 10.1103/PhysRevB.75.233410

[23] Onoe J, Ito T, Kimura S. Time dependence of the electronic structure of an electron-beam-irradiated C_{60} film. J Appl Phys. 2008;104(10):103706. doi: 10.1063/1.3028263

[24] Onoe J, Ito T, Shima H, et al. Observation of Riemannian geometric effects on electronic states. Europhys Lett. 2012;98(2):27001. doi: 10.1209/0295-5075/98/27001

[25] Masuda H, Onoe J, Yasuda H. High-resolution transmission electron microscopic and electron diffraction studies of C_{60} single crystal films before and after electron-beam irradiation. Carbon. 2015;81:842–846. doi: 10.1016/j.carbon.2014.09.049

[26] Masuda H, Yasuda H, Onoe J. Two-dimensional periodic arrangement of one-dimensional polymerized C_{60} evidenced by high-resolution cryo-transmission electron microscopy. Carbon. 2016;96:316–319. doi: 10.1016/j.carbon.2015.09.055

[27] Osawa E, Ho D. Nanodiamond and its application to drug delivery. J Med Allied Sci. 2012;2(2):31–40.

[28] Rehman A, Houshyar S, Wang X. Nanodiamond-based fibrous composites: a review of fabrication methods, properties, and applications. ACS Appl Nano Mater. 2021;4(3):2317–2332. doi: 10.1021/acsanm.1c00470

[29] Qin J-X, Yang X-G, Lv C-F, et al. Nanodiamonds: synthesis, properties, and applications in

nanomedicine. Mater Design. 2021;210:110091. doi: 10.1016/j.matdes.2021.110091
[30] Takashima A, Nishii T, Onoe J. Formation process and electron incident energy dependence of one-dimensional uneven peanut-shaped C_{60} polymer studied using *in situ* high-resolution infrared spectroscopy and first-principles density-functional calculations. J Phys D Appl Phys. 2012;45:485302. doi: 10.1088/0022-3727/45/48/485302
[31] Toda Y, Ryuzaki S, Onoe J. Femtosecond carrier dynamics in an electron-beam-irradiated C_{60} film. Appl Phys Lett. 2008;92(9):094102. doi: 10.1063/1.2838347
[32] Onoe J, Takashima A, Ono S, et al. Anomalous enhancement in the infrared phonon intensity of a one-dimensional uneven peanut-shaped C_{60} polymer. J Phys Condens Matter. 2012;24(17):175405. doi: 10.1088/0953-8984/24/17/175405
[33] Onoe J, Takashima A, Toda Y. Infrared phonon anomaly of one-dimensional metallic peanut-shaped C_{60} polymer. Appl Phys Lett. 2010;97(24):241911. doi: 10.1063/1.3527961
[34] Shima H, Yoshioka H, Onoe J. Geometry-driven shift in the Tomonaga-Luttinger exponent of deformed cylinders. Phys Rev B. 2009;79(20):201401. doi: 10.1103/PhysRevB.79.201401
[35] DeWitt BS. Point transformations in quantum mechanics. Phys Rev. 1952;85(4):653–661. doi: 10.1103/PhysRev.85.653
[36] Jansen H, Koppe H. Quantum mechanics with constraints. Ann Phys. 1971;63(2):586–591. doi: 10.1016/0003-4916(71)90031-5
[37] da Costa RCT. Quantum mechanics of a constrained particle. Phys Rev A. 1981;23(4):1982–1987. doi: 10.1103/PhysRevA.23.1982
[38] Tomonaga S. Remarks on Bloch's method of sound waves applied to many-Fermion problems. Prog Theor Phys. 1950;5(4):544–569. doi: 10.1143/ptp/5.4.544
[39] Luttinger JM. An exactly soluble model of a many-Fermion system. J Math Phys. 1963;4(9):1154–1162. doi: 10.1063/1.1704046
[40] Ishii H, Kataura H, Shiozawa H, et al. Direct observation of Tomonaga-Luttinger-liquid state in carbon nanotubes at low temperatures. Nature. 2003;426:540–544. doi: 10.1038/nature02074
[41] Noda Y, Ono S, Ohno K. Geometry dependence of electronic and energetic properties of one-dimensional peanut-shaped fullerene polymers. J Phys Chem A. 2015;119(12):3048–3055. doi: 10.1021/jp512451u
[42] Rauf H, Pichier T, Knupfer M, et al. Transition from a Tomonaga-Luttinger liquid to a fermi liquid in potassium-intercalated bundles of single-wall carbon nanotubes. Phys Rev Lett. 2004;93(9):096805. doi: 10.1103/PhysRevLett.93.096805
[43] Larciprete R, Petaccia L, Lizzit S, et al. Transition from one-dimensional to three-dimensional behavior induced by lithium doping in single wall carbon nanotubes. Phys Rev B. 2005;71(11):115435. doi: 10.1103/PhysRevB.71.115435
[44] Nakaya M, Watanabe S, Onoe J. Control of electrical, optical, and thermal properties of C_{60} films by electron-beam irradiation. Carbon. 2019;152:882–887. doi: 10.1016/j.carbon.2019.06.089
[45] Wang G, Li Y, Huang Y. Structures and electronic properties of peanut-shaped dimers and carbon nanotubes. J Phys Chem B. 2005;109(21):10957–10961. doi: 10.1021/jp050030u
[46] Ueda S, Ohno K, Noguchi Y, et al. Dimension dependence of the electronic structure of fullerene polymers. J Phys Chem B. 2006;110(45):22374–22381. doi: 10.1021/jp063458h
[47] Noda Y, Ohno K. Metallic and non-metallic properties of one-dimensional peanut-shaped fullerene polymers. Synth Met. 2011;161(15–16):1546–1551. doi: 10.1016/j.synthmet.2011.05.012
[48] Hassanien A, Gasprič J, Demsar J, et al. Atomic force microscope of photo-polymerized and photo-dimerized epitaxial C_{60} films. Appl Phys Lett. 1997;70(4):417–419. doi: 10.1063/1.118321
[49] Nakayama T, Onoe J, Nakatsuji K, et al. Photo-induced products in a C_{60} monolayer on Si(111)$\sqrt{3}$x$\sqrt{3}$R30°-Ag: an STM study. Surf Rev Lett. 1999;6(6):1073–1078. doi: 10.1142/S0218625X99001177
[50] Service RF. Is the terabit within reach? Science. 2006;314(5807):1868–1870. doi: 10.1126/science.314.5807.1868
[51] Bhat WA. Is a data-capacity gap inevitable in big data storage? Computer. 2018;51(9):54–62. doi: 10.1109/MC.2018.3620975
[52] Feng M, Gao L, Deng Z, et al. Reversible, erasable, and rewritable nanorecording on an H2 rotaxane thin film. J Am Chem Soc. 2007;129(8):2204–2205. doi: 10.1021/ja067037p
[53] Nakaya M, Tsukamoto S, Kuwahara Y, et al. Molecular scale control of unbound and bound C_{60} for topochemical ultradense data storage in an ultrathin C_{60} film. Adv Mater. 2010;22(14):1622–1625. doi: 10.1002/adma.200902960
[54] Ma Y, Wen Y, Song Y. Ultrahigh density data storage based on organic materials with SPM techniques. J Mater Chem. 2011;21(11):3522–3533. doi: 10.1039/C0JM02471F
[55] Nakaya M, Aono M, Nakayama T. Molecular-scale size tuning of covalently bound assembly of C_{60} molecules. ACS Nano. 2011;5(10):7830–7837. doi: 10.1021/nn201869g
[56] Ye C, Li M, Luo J, et al. Photo-induced amplification of readout contrast in nanoscale data storage. J Mater Chem. 2012;22(10):4299–4305. doi: 10.1039/C2JM14923K
[57] Li S, Shang Y, Zhao E, et al. Color-tunable and highly solid emissive AIE molecules: synthesis, photophysics, data storage and biological application. J Mater Chem C. 2015;3(14):3445–3451. doi: 10.1039/C4TC02691H
[58] Nakaya M, Aono M, Nakayama T. Ultrahigh-density data storage into thin films of fullerene molecules. Jpn J Appl Phys. 2016;55(11):1102B4. doi: 10.7567/JJAP.55.1102B4
[59] Ceze L, Nivala J, Strauss K. Molecular digital data storage using DNA. Nat Rev Genet. 2019;20(8):456–466. doi: 10.1038/s41576-019-0125-3
[60] Yang Q, Zhong T, Tu Z, et al. Design of single-molecule multiferroics for efficient ultrahigh-density nonvolatile memories. Adv Sci. 2019;6(1):1801572. doi: 10.1002/advs.201801572
[61] Arcadia CE, Kennedy E, Geiser J, et al. Multicomponent molecular memory. Nat Commun. 2020;11(1):691. doi: 10.1038/s41467-020-14455-1
[62] Maeda K, Nakamura Y. Spreading effects in surface reactions induced by tunneling current injection from an STM tip. Surf Sci. 2003;528(1–3):110–114. doi: 10.1016/S0039-6028(02)02618-3

[63] Nakamura Y, Kagawa F, Kasai K, et al. Nonthermal decomposition of C_{60} polymers induced by tunneling electron injection. Appl Phys Lett. 2004;85 (22):5242–5244. doi: 10.1063/1.1825618
[64] Nakamura Y, Mera Y, Maeda K. Role of intermolecular separation in nanoscale patterning C_{60} films by local injection of electrons from scanning tunneling microscope tip. Jpn J Appl Phys. 2005;44(10L):L1373. doi: 10.1143/JJAP.44.L1373
[65] Nakaya M, Kuwahara Y, Aono M, et al. Reversibility-controlled single molecular level chemical reaction in a C_{60} monolayer via ionization induced by scanning transmission microscopy. Small. 2008;4(5):538–541. doi: 10.1002/smll.200701242
[66] Nakaya M, Kuwahara Y, Aono M, et al. Nanoscale control of reversible chemical reaction between fullerene C_{60} molecules using scanning tunneling microscope. J Nanosci Nanotechnol. 2011;11 (4):2829–2835. doi: 10.1166/jnn.2011.3898
[67] Núñez-Regueiro M, Marques L, Hodeau J-L, et al. Polymerized fullerite structures. Phys Rev Lett. 1995;74(2):278–281. doi: 10.1103/PhysRevLett.74.278
[68] Tsukamoto S, Nakaya M, Caciuc V, et al. Local dimerization and dedimerization of C_{60} molecules under a tip of scanning tunneling microscope: a first-principles study. Carbon. 2020;159:638–647. doi: 10.1016/j.carbon.2019.12.046
[69] Wang Y, Holden JM, Bi X-X, et al. Thermal decomposition of polymeric C_{60}. Chem Phys Lett. 1994;217 (4):413–417. doi: 10.1016/0009-2614(93)E1409-A
[70] Rao AM, Zhou P, Wang K-A, et al. Photoinduced polymerization of solid C_{60} films. Science. 1993;259 (5097):955–957. doi: 10.1126/science.259.5097.955
[71] Kalff F, Rebergen M, Fahrenfort E, et al. A kilobyte rewritable atomic memory. Nat Nanotech. 2016;11 (11):926–929. doi: 10.1038/nnano.2016.131
[72] Church GM, Gao Y, Kosuri S. Next-generation digital information storage in DNA. Science. 2012;337 (6102):1628. doi: 10.1126/science.1226355
[73] Erlich Y, Zielinski D. DNA fountain enables a robust and efficient storage architecture. Science. 2017;355 (6328):950–954. doi: 10.1126/science.aaj2038
[74] D'Alessandro DM, Smit B, Long JR. Carbon dioxide capture: prospects for new materials. Angew Chem Int Ed. 2010;49(35):6058–6082. doi: 10.1002/anie.201000431
[75] Beletskaya I, Tyurin VS, Tsivadze AYU, et al. Supramolecule chemistry of metalloporphrins. Chem Rev. 2009;109(5):1659–1713.
[76] Choi S, Drese JH, Jones CW. Adsorbent materials for carbon dioxide capture from large anthropogenic point sources. ChemSuschem. 2009;2(9):796–854. doi: 10.1002/cssc.200900036
[77] Matile S, Jentzsch AV, Montenegro J, et al. Recent synthetic transport systems. Chem Soc Rev. 2011;40 (5):2453–2474. doi: 10.1039/C0CS00209G
[78] Kitagawa S, Kitaura R, Noro S. Functional porous coordination polymers. Angew Chem Int Ed. 2004;43(18):2334–2375. doi: 10.1002/anie.200300610
[79] Matsuda R, Kitaura R, Kitagawa S, et al. Highly controlled acetylene accommodation in a metal-organic microporous materials. Nature. 2005;436:238–241. doi: 10.1038/nature03852
[80] Duan J, Higuchi M, Horike S, et al. High CO_2/CH_4 and C2 hydrocarbons/CH_4 selectivity in a chemically robust porous coordination polymer. Adv Funct Mater. 2013;23(28):3525–3530. doi: 10.1002/adfm.201203288
[81] Yang Y-W, Sun Y-L, Song N. Switchable host-guest systems on surfaces. Chem Res. 2014;47 (7):1950–1960. doi: 10.1021/ar500022f
[82] Nakaya M, Kitagawa Y, Watanabe S, et al. CO_2 immobilization at room temperature using the specific sub-nm space of one-dimensional uneven-structured C_{60} polymer films. Adv Sustain Sys. 2021;5 (1):2000156.
[83] Moore MH, Khanna RK. Infrared and mass spectra studies of proton irradiated H_2O+CO_2 ice: evidence for carbonic acid. Spectrochim Acta. 1991;47A:255–262. doi: 10.1016/0584-8539(91)80097-3
[84] Luz Z, Meiboom S. A DFT study of the water-assisted intramolecular proton transfer in the tautomers of adenine. J Phys Chem A. 1999;103(15):2744–2750. doi: 10.1021/jp982713y
[85] Khezri B, Fisher AC, Pumera M. CO_2 reduction: the quest for electrocatalytic materials. J Mater Chem A. 2017;5(18):8230–8246. doi: 10.1039/C6TA09875D
[86] Stuckert NR, Yang RT. CO_2 capture from the atmosphere and simultaneous concentration using zeolites and amine-grafted SBA-15. Environ Sci Technol. 2011;45(23):10257–10264. doi: 10.1021/es202647a
[87] Franco F, Rettenmaier C, Jeon HS, et al. Transition metal-based catalysts for the electrochemical CO_2 reduction: from atoms and molecules to nanostructured materials. Chem Soc Rev. 2020;49 (19):6884–6946. doi: 10.1039/D0CS00835D
[88] Shah SSA, Javed MS, Najam T, et al. Metal oxides for the electrocatalytic reduction of carbon dioxide: mechanism of active sites, composites, interface and defect engineering strategies. Coord Chem Rev. 2022;471:214716. doi: 10.1016/j.ccr.2022.214716
[89] Adabala S, Dutta DP. A review on recent advances in metal chalcogenide-based photocatalysts for CO_2 reduction. J Environ Chem Eng. 2022;10(3):107763. doi: 10.1016/j.jece.2022.107763
[90] Liu K-G, Bigdeli F, Panjehpour A, et al. Metal organic framework composites for reduction of CO_2. Coord Chem Rev. 2023;493:215257. doi: 10.1016/j.ccr.2023.215257
[91] Zhao T, Wang Q, Kawazoe Y, et al. A metallic peanut-shaped carbon nanotube and its potential for CO_2 capture. Carbon. 2018;132:249–256. doi: 10.1016/j.carbon.2018.02.061
[92] Zhou W, Shen H, Wang Q, et al. N-doped peanut-shaped carbon nanotubes for efficient CO_2 electrocatalytic reduction. Carbon. 2019;152:241–246. doi: 10.1016/j.carbon.2019.05.078
[93] Hammes-Schiffer S, Stuchebrukhov AA. Theory of coupled electron and proton transfer reactions. Chem Rev. 2010;110(12):6939–6960. doi: 10.1021/cr1001436
[94] Sun X, Zhu Q, Kang X, et al. Molybdenum-bismuth bimetallic chalcogenide nanosheets for highly efficient electrocatalytic reduction of carbon dioxide to methanol. Angew Chem Int Ed. 2016;55 (23):6771–6775.
[95] Kuhl KP, Cave ER, Abram DN, et al. New insights into the electrochemical reduction of carbon dioxide on metallic copper surfaces. Ener Environ Sci. 2012;5(5):7050–7059. doi: 10.1039/C2EE21234J

[96] Ren D, Fong J, Yeo BS. The effects of currents and potentials on the selectivities of copper toward carbon dioxide electroreduction. Nat Commun. 2018;9 (1):925. doi: 10.1038/s41467-018-03286-w
[97] Sun J, Yuan K, Zhou W, et al. Low thermal conductivity of peanut-shaped carbon nanotube and its insensitive response to uniaxial strain. Nanotechnology. 2020;31(11):115701. doi: 10.1088/1361-6528/ab5b2c
[98] Sun J, Chen Y, Wang Q. Low lattice thermal conductivity of a 5-8-peanut-shaped carbon nanotube. Phys Chem Chem Phys. 2021;23(9):5460–5466. doi: 10.1039/D0CP06390H
[99] Hou L, Cui X, Guan B, et al. Synthesis of a monolayer fullerene network. Nature. 2022;606(7914):507–510. doi: 10.1038/s41586-022-04771-5
[100] Okada S, Saito S. Electronic structure and energetics of pressure-induced two-dimensional C_{60} polymers. Phys Rev B. 1999;59(3):1930–1936. doi: 10.1103/PhysRevB.59.1930
[101] Kremer RK, Rabenau T, Maser WK, et al. High-temperature conductivity study on single-crystal C_{60}. Appl Phys A. 1993;56(3):211–214. doi: 10.1007/BF00539476
[102] Ryuzaki S, Nishiyama M, Onoe J. Electron transport properties of air-exposed one-dimensional uneven peanut-shaped C_{60} polymer films. Diamond Relat Mater. 2013;33:12–15. doi: 10.1016/j.diamond.2012.12.004
[103] Ryuzaki S, Onoe J. Anomaly in the electronic resistivity of one-dimensional uneven peanut-shaped C_{60} polymer film at a low temperature. Appl Phys Lett. 2014;104(11):113301. doi: 10.1063/1.4869120
[104] Huang DL, Dau PD, Liu HT, et al. High-resolution photoelectron imaging of cold $C_{60}^-C_{60}^-$ anions and accurate determination of the electron affinity of C_{60}. J Chem Phys. 2014;140(22):224315.
[105] Ryuzaki S, Onoe J. Basic aspects for improving the energy conversion efficiency of hetero-junction organic photovoltaic cells. Nano Rev. 2013;4 (1):21055. doi: 10.3402/nano.v4i0.21055
[106] Ryuzaki S, Onoe J. Influence of charge accumulation of photogenerated carriers in the vicinity of donor/acceptor interface on the open-circuit voltage of zinc-porphyrin/C_{60} heterojunction organic photovoltaic cells. J Phys D Appl Phys. 2011;44:265102. doi: 10.1088/0022-3727/44/26/265102
[107] Kojima H, Abe R, Ito M, et al. Giant seebeck effect in pure fullerene thin films. Appl Phys Exp. 2015;8 (12):121301. doi: 10.7567/APEX.8.121301
[108] Yu RC, Tea N, Salamon MB, et al. Thermal conductivity of single crystal C_{60}. Phys Rev Lett. 1992;68 (13):050–2053.
[109] Han MK, Jin Y, Lee DH, et al. Thermoelectric properties of Bi2Te3: cul and the effect of its doping with PB atoms. Materials. 2017;10(11):1235.
[110] Culter M, Mott NF. Observation of Anderson localization in an electron gas. Phys Rev. 1969;181 (3):1336–1340. doi: 10.1103/PhysRev.181.1336
[111] Stepniak F, Benning PJ, Poirier DM, et al. Electrical transport in Na, K, Rb, and Cs fullerides: phase formation, microstructure, and metallicity. Phys Rev B. 1993;48(3):1899–1906. doi: 10.1103/PhysRevB.48.1899
[112] Menke T, Ray D, Meiss J, et al. *In-situ* conductivity and Seebeck measurements of highly efficient n-dopants in fullerene C_{60}. Appl Phys Lett. 2012;100 (9):093304. doi: 10.1063/1.3689778
[113] Suh J, Yu KM, Fu D, et al. Simultaneous enhancement of electrical conductivity and themopower of Bi2Te3 by multifunctionality of native defects. Adv Mater. 2015;27(24):3681.
[114] Kong S, Wu T, Yuan M, et al. Dramatically enhanced thermoelectric performance of MoS_2 by introducing MoO_2 nanoinclusions. J Mater Chem A. 2017;5 (5):2004–2011. doi: 10.1039/C6TA10219K
[115] Meletov KP, Arvanitidis J, Christofilos D, et al. Raman study of the temperature-induced decomposition of the fullerene dimers C_{120}. Chem Phys Lett. 2016;654:81–85. doi: 10.1016/j.cplett.2016.05.016
[116] Meletov KP, Arvanitidis J, Christofilos D, et al. Raman study of the temperature-induced decomposition of the two-dimensional rhombohedral polymer of C_{60} and the intermediate states formed. Carbon. 2010;48 (10):2974–2979. doi: 10.1016/j.carbon.2010.04.039
[117] Izumi T, Nakaya M, Onoe J. Kinetic study of photopolymerization and depolymerization in C_{60} films using *in situ* Fourier-transform infrared spectroscopy for develoment of C_{60}-based thermoelectric materials. Chem Phys Lett. 2022;801:139744. doi: 10.1016/j.cplett.2022.139744
[118] Nakaya M, Onoe J. Unpublished data.
[119] Smith BW, Monthioux M, Luzzi DE. Encapsulated C_{60} in carbon nanotubes. Nature. 1998;396 (6709):323–324. doi: 10.1038/24521
[120] Yudasaka M, Ajima K, Suenaga K, et al. Nano-extraction and nano-condensation for C_{60} incorporation into single-wall carbon nanotubes in liquid phases. Chem Phys Lett. 2003;380(1–2):42–46. doi: 10.1016/j.cplett.2003.08.095
[121] Simon F, Monthioux M. Carbon meta-nanotubes: synthesis, properties, and applications. New York, NY: John Wiley & Sons Ltd.; 2012. p. 273–322.
[122] Li YF, Kaneko T, Hatakeyama R. Electrical transport properties of fullerene peapods interacting with light. Nanotechnology. 2008;19(41):415201. doi: 10.1088/0957-4484/19/41/415201
[123] Yang J, Lee J, Lee J, et al. Conductivity and field emission enhancement of C_{60}-encapsulated single-walled carbon nanotubes. Diam Relat Mater. 2018;89:273–281. doi: 10.1016/j.diamond.2018.09.016
[124] Cui L, Feng Y, Zhang X. Dependence of thermal conductivity of carbon nanopeapods on filling ratios of fullerene molecules. J Phys Chem A. 2015;119 (45):11226–11232. doi: 10.1021/acs.jpca.5b07995
[125] Kataura H, Maniwa Y, Abe M, et al. Optical properties of fullerene and non-fullerene peapods. Appl Phys A. 2002;74(3):349–354. doi: 10.1007/s003390201276
[126] Shimada T, Ohno Y, Okazaki T, et al. Transport properties of C_{78}, C_{90} and Dy@C_{82} fullerenes-nanopepods by field effect transistors. Physica E. 2004;21(2–4):1089–1092.
[127] Simon F, Kuzmany H, Náfrádi B, et al. Magnetic fullerenes inside single-wall carbon anotubes. Phys Rev Lett. 2006;97(13):136801.
[128] Hirahara K, Suenaga K, Bandow S, et al. One-dimensional metallofullerene crystal generated inside single-walled carbon nanotubes. Phys Rev Lett. 2000;85(25):5384–5387. doi: 10.1103/PhysRevLett.85.5384
[129] Nakanishi R, Satoh J, Katoh K, et al. $DySc_2$@C_{80} single-molecule magnetic metallofullerene encapsulated in a single-walled carbon nanotube. J Am Chem Soc. 2018;140(35):10955–10959.

[130] Bandow S, Takizawa M, Hirahara K, et al. Raman scattering study of double-wall carbon nanotubes derived from the chains of fullerenes in single-wall carbon nanotubes. Chem Phys Lett. 2001;337(1–3):48–54. doi: 10.1016/S0009-2614(01)00192-0
[131] Pichler T, Kuzmany H, Kataura H, et al. Metallic polymers of C_{60} inside single-walled carbon nanotubes. Phys Rev Lett. 2001;87(26):267401. doi: 10.1103/PhysRevLett.87.267401
[132] Nakamura E. Atomic-resolution transmission electron microscopic movies for study of organic molecules, assemblies, and reactions: the first 10 years of development. Acc Chem Res. 2017;50(6):1281–1292. doi: 10.1021/acs.accounts.7b00076
[133] Shimizu T, Lungerich D, Harano K, et al. Time-resolved imaging of stochastic cascade reactions over a submillisecond to second time range at the angstrom level. J Am Chem Soc. 2022;144(22):9797–9805. doi: 10.1021/jacs.2c02297
[134] Okada S, Kowashi S, Schweighauser L, et al. Direct microscopic analysis of individual C_{60} dimerization events: kinetics and mechanisms. J Am Chem Soc. 2017;139(50):18281–18287. doi: 10.1021/jacs.7b09776
[135] Liu D, Kowashi S, Nakamuro T, et al. Ionization and electron excitation of C_{60} in a carbon nanotube: a variable temperature/voltage transmission electron microscopic study. Proc Natl Acad Sci USA. 2022;119(15):e2200290119. doi: 10.1073/pnas.2200290119
[136] Noda Y, Ono S, Ohno K. Metallic three-coordinated carbon networks with eight-membered rings showing high density of states at the Fermi level. Phys Chem Chem Phys. 2014;16(15):7102–7107. doi: 10.1039/C4CP00159A
[137] Ma J, Alfè D, Michaelides A, et al. Stone-wales defects in graphene and other planar sp^2-bonded materials. Phys Rev B. 2009;80(3):033407. doi: 10.1103/PhysRevB.80.033407
[138] Yazyev OV, Louie SG. Topological defects in graphene: dislocations and grain boundaries. Phys Rev B. 2010;81(19):195420. doi: 10.1103/PhysRevB.81.195420
[139] Andersen OK. Electronic structure of the fcc transition metals Ir, Rh, Pt, and Pd. Phys Rev B. 1970;2(4):883–906. doi: 10.1103/PhysRevB.2.883
[140] Chen H, Brener NE, Callaway J. Electronic structure, optical and magnetic properties of fcc palladium. Phys Rev B. 1989;40(3):1443–1449. doi: 10.1103/PhysRevB.40.1443
[141] Theileis V, Bross H. Relativistic modified augmented plane wave method and its application to the electronic structure of gold and palladium. Phys Rev B. 2000;62(20):13338–13346. doi: 10.1103/PhysRevB.62.13338
[142] Zhang S, Zhou J, Wang Q, et al. Penta-graphene: a new carbon allotrope. Proc Natl Acad Sci USA. 2015;112(8):2372–2377. doi: 10.1073/pnas.1416591112
[143] Shen Y, Wang Q. Pentagon-based 2D materials: classification, properties and applications. Phys Rep. 2022;964:1–42. doi: 10.1016/j.physrep.2022.03.003
[144] Nazir MA, Hassan A, Shen Y, et al. Research progress on penta-graphene and its related materials: properties and applications. Nano Today. 2022;44:101501. doi: 10.1016/j.nantod.2022.101501
[145] Wang H, Ding N, Jiang T, et al. Investigation on electronic and mechanical properties of penta-graphene nanotubes. J Mater Sci. 2020;55(29):14336–14344. doi: 10.1007/s10853-020-05035-1
[146] De Sousa JM, Aguiar A, Girão E, et al. Mechanical properties of single-walled penta-graphene-based nanotubes: a DFT and classical molecular dynamics study. Chem Phys. 2021;547:111187. doi: 10.1016/j.chemphys.2021.111187
[147] De Sousa JM, Botari T, Perim E, et al. Mechanical and structural properties of graphene-like carbon nitride sheets. RSC Adv. 2016;6(80):76915–76921. doi: 10.1039/C6RA14273G
[148] De Sousa JM, Aguiar AL, Girão EC, et al. Mechanical properties of pentagraphene-based nanotubes: a molecular dynamics study. MRS Adv. 2018;3(1–2):97–102. doi: 10.1557/adv.2018.160
[149] Chen M, Zhan H, Zhu Y, et al. Mechanical properties of penta-graphene nanotubes. J Phys Chem C. 2017;121(17):9642–9647. doi: 10.1021/acs.jpcc.7b02753
[150] Popov V, Van Doren V, Balkanski M. Elastic properties of single-walled carbon nanotubes. Phys Rev B. 2000;61(4):3078–3084. doi: 10.1103/PhysRevB.61.3078
[151] De Sousa JM, Aguiar A, Girão E, et al. Elastic and fracture properties of single walled pentagraphene nanotubes. arXiv:1911.12251. 2019. doi: 10.48550/arXiv.1911.12251
[152] Wang Z, Cao X, Qiao C, et al. Novel penta-graphene nanotubes: strain-induced structural and semiconductor-metal transitions. Nanoscale. 2017;9(48):19310–19317.
[153] Shah K, Parvaiz MS, Dar GN. Porous pentagraphene nanotube halogen gas sensor: a first principles study. Adv Nat Sci Nanosci Nanotechnol. 2023;14(2):025016. doi: 10.1088/2043-6262/acd92c
[154] Kuklin AV, Ågren H, Avramov PV. Structural stability of single-layer $PbSe_2$ with pentagonal puckered morphology and its nanotubes. Phys Chem Chem Phys. 2020;22(16):8289–8295. doi: 10.1039/D0CP00979B
[155] Ati AH, Cheng JW, Sun Q. A computational study of hydrogen adsorption on penta-NiN_2 sheet and nanotubes. Int J Hydrogen Energy. 2023;52:191–198. doi: 10.1016/j.ijhydene.2023.06.120
[156] Kobata Y, Matsutani S, Noda Y, et al. A novel symmetry in nanocarbons: pre-constant discrete principal curvature structure. arXiv: 2306.15839. 2023. doi: 10.48550/arXiv.2306.15839
[157] Mackay AL, Terrones H. Diamond from graphite. Nature. 1991;352(6338):762. doi: 10.1038/352762a0
[158] Lenosky T, Gonze X, Teter M, et al. Energetics of negatively curved graphitic carbon. Nature. 1992;355(6358):333–335. doi: 10.1038/355333a0
[159] Tagami M, Liang Y, Naito H, et al. Negatively curved cubic carbon crystals with octahedral symmetry. Carbon. 2014;76:266–274. doi: 10.1016/j.carbon.2014.04.077
[160] Park N, Yoon M, Berber S, et al. Magnetism in all-carbon nanostructures with negative Gaussian curvature. Phys Rev Lett. 2003;91(23):237204. doi: 10.1103/PhysRevLett.91.237204